

Probing star formation in five of the most massive spiral galaxies observed through *ASTROSAT* UltraViolet Imaging Telescope

Shankar Ray,^{1,2*} Suraj Dhiwar,^{3,4} Joydeep Bagchi,¹ and M. B. Pandge^{2,†}

¹Department of Physics and Electronics, Christ University, Hosur Road, Bengaluru 560029, India

²Department of Physics and Electronics, Dayanand Science College, Latur 413512, India

³Inter-University Centre for Astronomy and Astrophysics, Pune 411007, India

⁴Savitribai Phule Pune University, Pune 411007, India

Accepted XXX. Received YYY; in original form ZZZ

ABSTRACT

We present highly resolved and sensitive imaging of the five nearby massive spiral galaxies (with rotation velocities $> 300\text{kms}^{-1}$) observed by the UltraViolet Imaging Telescope onboard India’s multi-wavelength astronomy satellite *ASTROSAT*, along with other archival observations. These massive spirals show a far-ultraviolet star formation rate in the range of $\sim 1.4\text{--}13.7\text{M}_{\odot}\text{yr}^{-1}$ and fall in the ‘Green Valley’ region with a specific star formation rate within $\sim 10^{-11.5}\text{--}10^{-10.5}\text{yr}^{-1}$. Moreover, the mean star formation rate density of the highly resolved star-forming clumps of these objects are in the range $0.011\text{--}0.098\text{M}_{\odot}\text{yr}^{-1}\text{kpc}^{-2}$, signifying localised star formation. From the spectral energy distributions, under the assumption of a delayed star formation model, we show that the star formation of these objects had peaked in the period of $\sim 0.8\text{--}2.8$ Gyr after the ‘Big Bang’ and the object that has experienced the peak sooner after the ‘Big Bang’ show relatively less star-forming activity at $z\sim 0$ and falls below the main-sequence relation for a stellar content of $\gtrsim 10^{11}\text{M}_{\odot}$. We also show that these objects accumulated much of their stellar mass in the early period of evolution with $\sim 31\text{--}42$ per cent of the total stellar mass obtained in a time of $(1/16)\text{--}(1/5)^{\text{th}}$ the age of the Universe. We estimate that these massive objects convert their halo baryons into stars with efficiencies falling between $\sim 7\text{--}31$ percent.

Key words: galaxies: ISM – Galaxy: formation – galaxies: spiral – Galaxy: fundamental parameters – galaxies: individual: NGC 1030, NGC 1961, NGC 4501, NGC 5635, NGC 266

1 INTRODUCTION

Significant progress over the past few decades has been made in the understanding of the formation of galaxies and their evolution with time. However, a fully developed theory of galaxy formation remains one of the significant frontier problems of astrophysics (see Gott 1977; Brodie & Strader 2006; Somerville & Davé 2015; Naab & Ostriker 2017; Robertson 2022 for a review of galaxy formation theories, also see White & Rees 1978; White & Frenk 1991; Fukugita & Peebles 2006; Sommer-Larsen 2006; Cole et al. 2000 for some leading works on galaxy formation). Moreover, explaining galaxy formation and evolution across cosmic time involves understanding processes across many branches of physics, starting from cosmology to plasma physics, which necessarily span a vast range of lengths and timescales. The current galaxy formation scenario is discussed under the hierarchical structure formation model of lambda cold dark matter cosmology ΛCDM (see Benson 2010 for a review). Specifically, it is still uncertain how and when the rare, incredibly massive, rotationally supported spiral galaxies observed in the local Universe, with stellar masses $> 10^{11}\text{M}_{\odot}$ and viral masses $> 10^{13}\text{M}_{\odot}$, have formed, as it depends on poorly understood non-linear

baryonic physics and complex interaction with the dark matter halos. However, based on cosmological simulations, Oser et al. (2010) propose a ‘two-phase’ evolution of galaxies consisting of a rapid early phase in $z \gtrsim 2$ followed by an extended phase of evolution for $z \lesssim 3$. They suggest that progenitor of massive galaxies grew considerably in the extended phase by accreting and merging with smaller satellite galaxies formed even before $z \sim 3$ around the gravitational well of the central galaxy (see Lackner et al. 2012; Rodriguez-Gomez et al. 2016 also). They also emphasise that the massive galaxies have a considerably higher population of older stars, which is a result of merging with systems that already had ‘in situ’ star formation before $z \sim 2$ and they grew in physical dimension according to hierarchical clustering as proposed by ΛCDM cosmology. Dekel et al. (2009) provide a theoretical background of the formation of massive galaxies at high red-shift, where the interplay between smooth, clumpy cold streams, instability in the disc and bulge formation govern the growth and evolution of the early phase of the galaxies.

Recent observations have found the existence of massive galaxies at the early Universe. For instance, Labbe et al. (2022) reported the finding of six massive galaxies with stellar mass $\gtrsim 10^{10}\text{M}_{\odot}$ at red-shift $7.4 \leq z \leq 9.1$, Huang et al. (2023) reported the existence of Ultra Luminous Infrared Galaxies (ULIRG) with infrared luminosity $L_{\text{IR}} > 10^{12.5}L_{\odot}$ and stellar masses $\sim 10^{11}\text{M}_{\odot}$ at red-shift $z \sim 2$, Cheng et al. (2023) found 16 galaxies with stellar mass $> 10^{10.5}\text{M}_{\odot}$

* E-mail: shankarray.physics@gmail.com

† E-mail: mbpandge@gmail.com

at red-shift $1 < z < 4.5$. All these findings indicate that some of these objects had experienced a period of intense star formation and stellar mass growth in a very short period of time in the early Universe. However, the general trend for galaxies, verified by observations, has been that the star formation rate reached its peak at the ‘cosmic high noon’ or ‘cosmic noon’ near redshift $z \approx 1 - 2$ when galaxies were rapidly building up their stellar masses by converting cosmic baryons to stars, and subsequently, over the next few billions of years the star formation went down drastically (Madau & Dickinson 2014).

Eventually, by the present era, most of the massive galaxies are supposed to have stopped growing (Brinchmann et al. 2004; Renzini & Peng 2015), having reached a state of apparent quiescence (Behroozi et al. 2010, 2019; Moster et al. 2013). And, for reasons still unknown, in our local universe, some low-mass galaxies are still actively forming stars, while the majority of massive galaxies with halo masses $M_{\text{halo}} \gtrsim 10^{12} M_{\odot}$ display a strikingly low specific star formation rate $s\text{SFR}$ (where $s\text{SFR} = \text{SFR}/\text{stellar mass}$; SFR being the star formation rate) compared to less massive galaxies (see Alexander & Hickox (2012) and Wechsler & Tinker (2018) for reviews). One such extremely massive, low star formation rate, ‘red and dead’ spiral galaxy UGC 12591, was reported in Ray et al. (2022).

The suppression of star formation in these galaxies could be due to multiple factors contributing together and/or functional over different timescales of galaxies’ evolution. Further, different quenching mechanisms may dominate at different mass ranges of galaxies (Kaviraj et al. 2007; Cicone et al. 2014; Förster Schreiber et al. 2014; Dhiwar et al. 2023). For massive galaxies with halo mass $\gtrsim 10^{12} M_{\odot}$, the halo gas gets shocked heated (Rees & Ostriker 1977) while collapsing onto the dark matter halo, which can delay the star-forming activity in the host galaxy’s disc (Birnboim & Dekel 2003). For massive galaxies at high red-shift $z \sim 2$, Feldmann & Mayer (2015) show that the suppression of star formation happens due to reduced accretion of gas from the intergalactic medium to the galactic dark matter halo, termed as ‘Cosmological Starvation’ and suggest the presence of additional mechanism such as radio-mode feedback to maintain the quenched state up to the present times (Bower et al. 2006; Croton et al. 2006). Park et al. (2023) found that the massive galaxies at the ‘cosmic noon’ are formed from a major starburst and are rapidly quenched by AGN feedback. While, from the morphological analysis of the star-forming regions of galaxies with stellar masses $> 10^{11.3} M_{\odot}$, Xu et al. (2020) conclude that one-fifth of the massive galaxies are still forming stars, and overwhelmingly most of them have gone through recent mergers.

Moreover, massive galaxies with rotational velocities $v_{\text{rot}} \gtrsim 300 \text{ km s}^{-1}$ tend to deviate from the baryonic Tully-Fisher relation, a tight scaling relation between the baryonic mass content and flat rotational velocity of a galaxy (McGaugh 2005), as shown in Ogle et al. (2019b); Dai et al. (2012); Ray et al. (2022). For example, the massive spirals like NGC 1961 and NGC 6753 (stellar mass $\gtrsim 10^{11} M_{\odot}$) with moderate star formation of $\sim 15.5 M_{\odot} \text{ yr}^{-1}$ and $\sim 11.8 M_{\odot} \text{ yr}^{-1}$ respectively are reported to contain $\sim 30 - 50$ per cent fewer baryons in their halos than what is expected from the cosmic baryon fraction (Bogdán et al. 2013a). Similarly, another massive disc galaxy UGC 12591 contains ~ 85 per cent fewer baryons than that expected from the cosmic mean having a star formation rate of $\sim 0.638 M_{\odot} \text{ yr}^{-1}$ (Ray et al. 2022). This deficiency in baryons in these galaxies also contributes to their deviations from the baryonic Tully-Fisher relation (Ray et al. 2022), emphasising their inability to condense halo baryons into stars. So, knowing the different assembly histories of such galaxies is extremely important, and to be able to constrain the star formation over the period, starting

from the early Universe, of such galaxies would give us a significant understanding of their evolution.

In this paper, we report the ultraviolet observations of five of the most massive spiral galaxies known, in combination with data at other wavelengths, to address some of the most critical questions in this field, like how the cooling of the circum-galactic gas effect star formation in such galaxies, how star formation is fuelled or quenched, and what are the dominant feedback mechanisms for quenching the star formation. These galaxies are extremely massive with stellar masses $> 10^{11} M_{\odot}$ and they also are fast rotators with rotational velocities $> 300 \text{ km s}^{-1}$. Here, we investigate the star formation history, nature of the star-forming regions, signatures and possible AGN/radiative feedback effects on the star formation, etc, accounting for the total baryon budget in these massive, fast-rotating spiral galaxies in the local Universe.

The structure of this paper is as follows: In §2, we describe the observations and data. The data reduction strategy for the UVIT observations, along with the hierarchical structuring of star-forming regions and Spectral Energy Distribution (SED) fitting processes taking FUV to FIR observations of the objects into account, are described in §3. In §4, we present our discussion, and the study’s conclusions are outlined in §5. Note that, in our discussion, we explore our objects through the parameters found from direct observations, scaling relations and also from fitting appropriate models to observable data. In our calculations we use the following cosmological parameters; $H_0 = 69.6 \text{ km s}^{-1} \text{ Mpc}^{-1}$, $\Omega_M = 0.286$ and $\Omega_{\text{vac}} = 0.714$.

2 DATA

2.1 Sample selection

Massive galaxies with high rotational velocities ($\gtrsim 300 \text{ km s}^{-1}$) have been under study for their departures from the long-established baryonic Tully-Fisher relation. In order to investigate their baryon-to-star conversion, we have observed five such extremely massive galaxies in UVIT (Table. 1) as a pilot sample with outer Keplerian disc rotation velocities $v_{\text{rot}} > 300 \text{ km s}^{-1}$ (Saglia & Sancisi (1988); Rubin et al. (1979); Corradi & Capaccioli (1991); Garrido et al. (2005), Table 2) for this study. These galaxies have K-band stellar masses $> 10^{11} M_{\odot}$ and virial masses $> 10^{13} M_{\odot}$ (see Table 2, Section 4.3 and Section 4.5). Previously, we published a detailed analysis of one such massive galaxy, UGC 12591 (Ray et al. 2022), which has $v_{\text{rot}} \approx 500 \text{ km s}^{-1}$. The target galaxies are late-type spirals in the morphological sequence characterised in HyperLeda (Makarov et al. 2014). To see their morphological appearances and other hidden features, we have made color images of these target galaxies in the optical band, which are shown in Fig. 1. These images are made using archival data of z, r and g bands from the Dark Energy Camera Legacy Survey (DECaLS), Panoramic Survey Telescope and Rapid Response System (Pan-STARRS) and Sloan Digital Sky Survey (SDSS). From Fig. 1, it is evident that the object NGC 266 has the face-on view with an inclination angle (the angle between the line of sight and the polar axis of the galaxy) of ~ 16 degree, and the other objects are almost edge-on with inclination angles of $\sim 47, 63, 68$ and 73 degrees for NGC 1961, NGC 4501, NGC 1030 and NGC 5635 respectively. Note that the inclination angles for our objects have opted from HyperLeda, where the apparent flattening (r_{25}) and morphological type (t) of a galaxy are used to find out the inclination (i) from the following relation,

Object	Band	Wavelength (λ) Å	Exposure time (sec)	Observation Id
NGC 1030	F154W	1541	1911.445	A05_225T04_9000002400
NGC 1961	F154W	1541	1900.023	A05_225T02_9000002510
NGC 4501	F154W	1541	1608.817	A04_167T05_9000002052
NGC 5635	F154W	1541	8068.550	A04_167T02_9000001974
NGC 5635	N242W	2418	8191.425	A04_167T02_9000001974
NGC 266	F154W	1541	7449.227	A04_167T04_9000001734
NGC 266	N242W	2418	7493.291	A04_167T04_9000001734

Table 1. The details of observations for the five massive spiral galaxies are mentioned here.

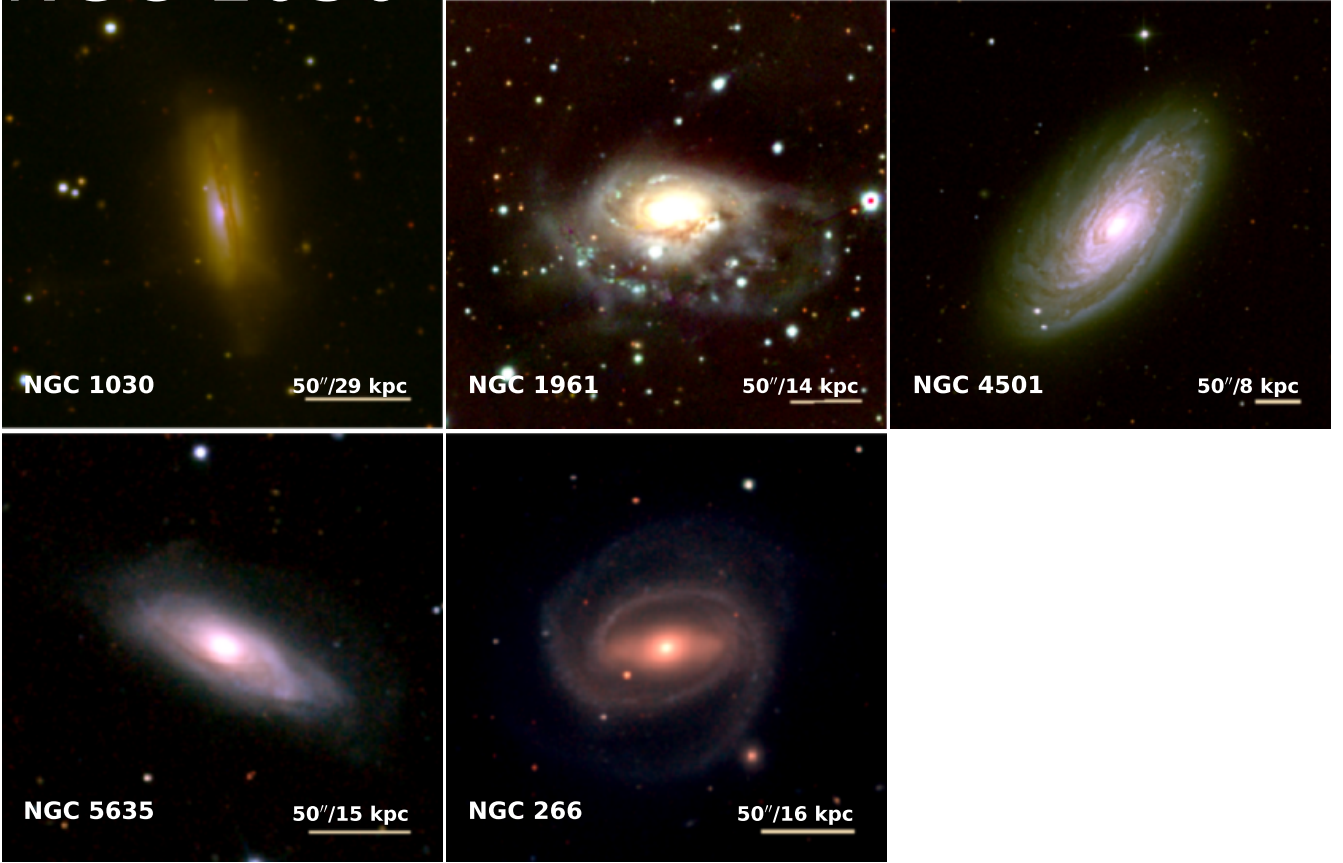


Figure 1. In the above figure, we show the RGB images of the five massive late-type spirals (Table 1). The images are made using optical data ($\sim 0.4 - 0.9\mu\text{m}$) in the following configurations: (a) NGC 1030: DECaLS z+r+g, (b) NGC 1961: PanSTARRS1 z+r+g, (c) NGC 4501: SDSS z+r+g, (d) NGC 5635: SDSS z+r+g and (e) NGC 266: SDSS z+r+g. Note that, the scale shown in the lower-right of each image is 50 arcsec.

$$\sin^2(i) = \frac{1 - 10^{-2\log(r_{25})}}{1 - 10^{-2\log(r_0)}} \quad (1)$$

where $\log(r_0) = 0.43 + 0.053t$ for $t = [-5, 7]$ and $\log(r_0) = 0.38$ for $t > 7$ (see HyperLeda for more details; Makarov et al. 2014). The dust lanes are clearly visible in NGC 1030 due to its edge on view. It has a rectangular shape with growing asymmetries visible at the edges (Lütticke et al. 2004). NGC 1961 is classified as an intermediate spiral galaxy, objects falling between barred and unbarred spiral galaxies in the morphological classification, with a bar not well defined, which is evident from the optical color image. The highly

asymmetric spiral arms of this object are signatures of possible strong recent interaction(s) (Gottesman et al. 1983), specifically due to the stripping of gas from the gravitational potential of the galaxy by $\sim 10^7\text{K}$ hot intergalactic medium as proposed by Shostak et al. (1982). Any asymmetry in NGC 4501 is not very dominant in the optical image. However, we can see the bright spiral arms embedded into dusty regions throughout the galaxy. However, Vollmer et al. (2008) show the existence of early-stage ram-pressure stripping in the galaxy. A clear asymmetry can be seen in the light distribution for the object NGC 5635, indicating possible recent interaction also shown by Saglia & Sancisi (1988). The tight-arm and barred spiral

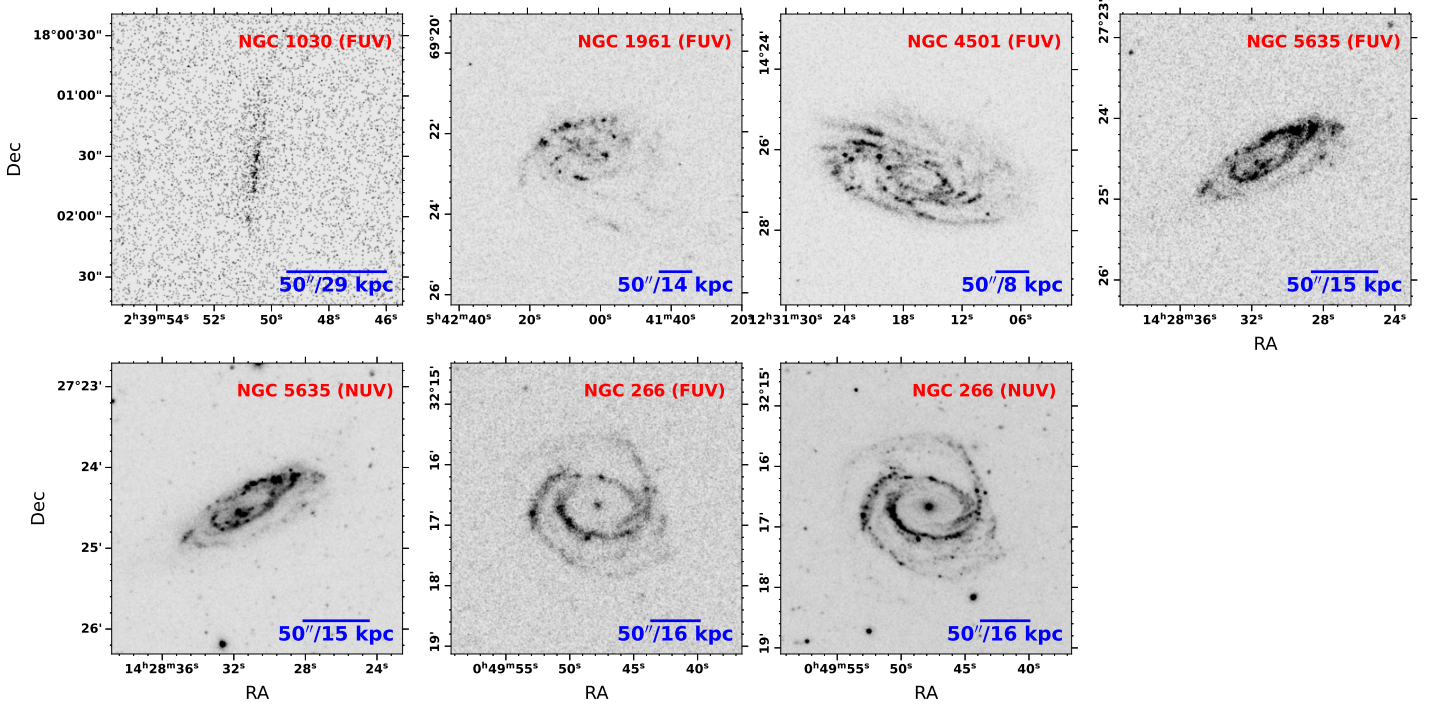


Figure 2. Here, in the above figure, we show the calibrated images of our objects from UVIT Level-1 data processed in CCDLAB (Postma & Leahy 2017). We have FUV F154W ($\sim 0.1541\mu\text{m}$) observations for all five spirals and NUV N242W ($\sim 0.2420\mu\text{m}$) observations for the objects NGC 5635 and NGC 266. In FUV band, the integration times of the objects are $T_{\text{int}} \sim 1.9, 1.9, 1.6, 8.1$ and 7.4 ks for NGC 1030, NGC 1961, NGC 4501, NGC 5635 and NGC 266 respectively. In NUV band, $T_{\text{int}} \sim 8.2, 7.5$ ks for NGC 5635 and NGC 266 respectively. Note that, the scale shown in the lower-right of each image is 50 arcsec.

galaxy NGC 266, which is part of a group consisting of six low mass galaxies (Bogdán et al. 2013a), is also found to be interacting with a Seyfert II galaxy Mrk 348 (Hibbard et al. 2001).

In Table 2, we show some important parameters for our sample galaxies. Some are obtained from the literature, shown in the upper panel of the table and these are coordinates of the objects (R.A., Dec.), morphological classification T, redshift z , flat rotational velocity v_{rot} (km s^{-1}), central velocity dispersion σ (km s^{-1}) and activity class β of the active galactic nuclei (AGN) of the objects. In the lower panel, we show a list of parameters derived in this work directly from observations or indirectly using scaling relations. The FUV and NUV magnitudes (m_{FUV} and m_{NUV}) of the objects are estimated using UVIT data within the apertures estimated following the process described in Section 3.2. The FUV star formation rates SFR_{FUV} are estimated using the corresponding FUV magnitudes/luminosities and the relation provided by Kennicutt (1998) for Salpeter initial mass function (IMF) (Salpeter 1955) (see Section 3.3). The star formation rates corrected for internal dust attenuation of the galaxies are denoted by $\text{SFR}_{\text{FUV}}^{\text{corr}}$ and are estimated considering the total infrared radiations into account following the process described in Section 4.1. The K-band mass to light ratios Y_K^* of the objects are calculated using specific colors (Section 4.3) and the scaling relations provided by Bell et al. (2003), and we have used them to calculate the K-band stellar masses M_K of our objects from 2MASS K-band luminosities. The specific star formation rates $s\text{SFR}_{\text{FUV}}^{\text{corr}}$ are calculated from the dust-corrected star formation rates and the K-band stellar masses as $\text{SFR}_{\text{FUV}}^{\text{corr}}/M_K$. The neutral hydrogen masses M_{HI} are calculated from 21cm integrated line flux following the relation provided in Section 4.3. On the other hand, the molecular hydrogen masses M_{H_2} are found out using the estimated neutral

hydrogen mass multiplied by scale factors provided by Young & Knezek (1989). The black hole masses M_{bh} are calculated indirectly from the central velocity dispersions σ or the stellar masses of the objects (see Section 4.4 for the relations used and the references). The halo masses M_{halo} are estimated under the assumption of flat circular velocity upto the virial radius within which the mean density is 200 times that of the critical density of the universe at that redshift (more on this in Section 4.5). T_{vir} denotes the temperature of the gas in the hot halo of the galaxies, which is considered to be a virialized system, calculated using the rotational velocity (see Section 4.3).

2.2 Observations

The data were taken by ASTROSAT UVIT under the proposals A04_167 and A05_225 (Principal Investigator Joydeep Bagchi). The objects are observed in the photon counting mode, and the details of the observations are tabulated in Table 1. The observations were carried out to study the young star formation in our objects. UVIT is a versatile instrument designed to see the sky in FUV ($130 \lesssim \lambda \lesssim 180$ nm), NUV ($200 \lesssim \lambda \lesssim 300$ nm) and in the Visible band (VIS) ($320 \lesssim \lambda \lesssim 550$ nm). UVIT is capable of making images simultaneously in a field of view of ~ 28 arcmins with a resolution of < 1.8 arcsec FWHM. In the two ultraviolet channels, gratings are provided for low-resolution (~ 100) slitless spectroscopy. The focusing optics is configured as twin R-C telescopes, each with a primary mirror with an effective diameter of ~ 37.5 centimetre. The FUV and NUV channels provide science observations, while the VIS channel mainly enables corrections for telescope drifts. The NUV and FUV channels provide excellent angular resolutions of ~ 1.2 and ~ 1.4 arcseconds, respectively, thereby much improving on their predecessor GALEX,

Parameters	Units	NGC 1030	NGC 1961	NGC 4501	NGC 5635	NGC 266
R.A.	–	02h 39m 50.600s	05h 42m 4.633s	12h 31m 59.153s	14h 28m 31.762s	00h 49m 47.815s
Dec.	–	+18d 01m 27.40s	+69d 22m 42.41s	+14d 25m 13.15s	+27d 24m 32.23s	+32d 16m 39.79s
T	–	Sc	SABb	Sb	Sb	Sab (Barred)
z	–	0.02851	0.01312	0.00762	0.01440	0.01550
v_{rot}	km s ⁻¹	371 ^a	402 ^b	320 ^c	386 ^a	363 ^d
σ	km s ⁻¹	–	242.8 ± 11.5	166.2 ± 7.1	–	229.1 ± 7.2
β	–	–	S3	S2	S3	S3b
m_{FUV}	mag	17.66 ± 0.01	14.33 ± 0.01	13.60 ± 0.01	16.18 ± 0.01	15.78 ± 0.01
m_{NUV}	mag	17.34 ± 0.05	13.49 ± 0.03	12.86 ± 0.03	15.87 ± 0.002	15.15 ± 0.002
Aperture	kpc ²	1.33 × 10 ⁴	1.01 × 10 ⁴	6.24 × 10 ³	7.77 × 10 ³	5.04 × 10 ³
SFR_{FUV}	M _⊙ yr ⁻¹	0.82 ± 0.01	4.00 ± 0.05	2.40 ± 0.02	0.80 ± 0.01	1.36 ± 0.02
$\text{SFR}_{\text{FUV}}^{\text{corr}}$	M _⊙ yr ⁻¹	5.15 ± 0.87	13.66 ± 2.04	13.51 ± 2.24	1.43 ± 0.13	2.54 ± 0.25
Y_{K}^*	M _⊙ /L _⊙	0.86	0.78	0.89	0.99	0.83
M_{K}	M _⊙	4.92 × 10 ¹¹	4.38 × 10 ¹¹	5.80 × 10 ¹¹	2.47 × 10 ¹¹	4.12 × 10 ¹¹
$\text{sSFR}_{\text{FUV}}^{\text{corr}}$	yr ⁻¹	(1.05 ± 0.18) × 10 ⁻¹¹	(3.12 ± 0.47) × 10 ⁻¹¹	(2.33 ± 0.39) × 10 ⁻¹¹	(0.58 ± 0.05) × 10 ⁻¹¹	(0.62 ± 0.06) × 10 ⁻¹¹
M_{HI}	M _⊙	1.32 × 10 ¹⁰	3.58 × 10 ¹⁰	7.09 × 10 ⁹	1.27 × 10 ¹⁰	7.99 × 10 ⁹
M_{H2}	M _⊙	(9.64 ± 1.72) × 10 ⁹	(7.88 ± 2.15) × 10 ¹⁰	(1.28 ± 0.21) × 10 ¹⁰	(2.29 ± 0.38) × 10 ¹⁰	(1.76 ± 0.48) × 10 ¹⁰
M_{gas}	M _⊙	(3.16 ± 0.24) × 10 ¹⁰	(1.58 ± 0.30) × 10 ¹¹	(2.75 ± 0.29) × 10 ¹⁰	(4.90 ± 0.52) × 10 ¹⁰	(3.55 ± 0.66) × 10 ¹⁰
M_{bh}	M _⊙	(1.45 ± 0.37) × 10 ⁸	(3.00 ± 0.60) × 10 ⁸	(6.01 ± 1.21) × 10 ⁷	(6.31 ± 1.48) × 10 ⁷	(2.34 ± 0.37) × 10 ⁸
M_{halo}	M _⊙	1.68 × 10 ¹³	2.16 × 10 ¹³	1.09 × 10 ¹³	1.91 × 10 ¹³	1.59 × 10 ¹³
T_{vir}	keV	0.43	0.50	0.32	0.46	0.41

Table 2. Here, in the upper panel of the table, we mention some properties related to the galaxies. The mentioned parameters are: R.A. = Right Ascension (J2000), Dec. = Declination (J2000), T = morphology, z = red-shift, v_{rot} = rotational velocity and, σ = central velocity dispersion and, β = activity class of AGN as per HyperLeda where S2, S3 and S3b denote Seyfert II, LINER and LINER with broad Balmer lines classes of AGNs respectively. In the lower panel, we mention the derived properties of our objects. The mentioned parameters are: m_{FUV} = FUV AB magnitude (corrected for foreground extinction), m_{NUV} = NUV AB magnitude (corrected for foreground extinction), A = aperture area, SFR_{FUV} = star formation rate, $\text{SFR}_{\text{FUV}}^{\text{corr}}$ = star formation rate from corrected FUV luminosity, Y_{K}^* = K-band stellar mass-to-light ratio, M_{K} = K-band stellar mass, $\text{sSFR}_{\text{FUV}}^{\text{corr}}$ = $\text{SFR}_{\text{FUV}}^{\text{corr}}/M_{\text{K}}$, specific star formation rate, M_{HI} = atomic hydrogen mass, M_{halo} = virial/halo mass, T_{vir} = virial temperature of the hot gas. The references for the rotational velocities v_{rot} are, a: [Saglia & Sancisi \(1988\)](#), b: [Rubin et al. \(1979\)](#), c: [Corradi & Capaccioli \(1991\)](#), d: [Garrido et al. \(2005\)](#).

which had a spatial resolution of ~ 5 arcseconds. Even though the pixel scale at the detector plane is ~ 0.42 arcsec/pixel, an onboard algorithm enables incoming photons to be localized on the detector plane with higher accuracy of $1/8^{\text{th}}$ of a pixel. Due to this higher resolution capability, UVIT is a powerful tool to observe the young star formation in galaxies in a well-resolved manner.

In this study, in addition to ASTROSAT UVIT data we have also used archival data from the following missions:

- (i) Galaxy Evolution Explorer (GALEX) (NUV)
- (ii) Sloan Digital Sky Survey (SDSS) (u, g, r, i, z)
- (iii) Dark Energy Camera Legacy Survey (DECaLS) (g, r, i)
- (iv) Panoramic Survey Telescope and Rapid Response System (Pan-STARRS) (g, r, i, z, y)
- (v) Two Micron All-Sky Survey (2MASS) (J, H, K)
- (vi) Wide-field Infrared Survey Explorer (WISE) (W1, W2, W3, W4) and
- (vii) Infrared Astronomical Satellite (IRAS) (IRAS1, IRAS2, IRAS3, IRAS4).

3 DATA REDUCTION AND ANALYSIS

3.1 UVIT Level-1 data reduction

We obtained the Level-1 (L1) data for our objects from the ASTROSAT data archive. We used CCDLAB provided by [Postma & Leahy \(2017\)](#) to make observational and detector-related corrections to the L1 data to make it useful for scientific purposes. The L1 files for a particular object contain a FITS binary extension involving a

table of the centroid list. Each L1 file may contain multiple observational frames of an object that may be unique or repetitive in nature for each filters.

The image processing by CCDLAB is described in brief as follows: (i) In the first step, all the L1 data files are extracted and checked for their scientific usefulness. All of the duplicate and non-useful data are exempted from further analysis. While observing an object, a short observation of the first 20 seconds is done to test the bright object detection. These observations do not contain enough information to be useful scientifically, and these data are disregarded. All of these are done automatically by CCDLAB. The underlying principle is to create unique subsets of data from the extracted L1 files for each filter based on frame number and frame time of the centroid list, (ii) satellite/telescope drift corrections performed by taking VIS channel observations into account, (iii) exposure array correction, and (iv) finding astrometric solution of World Coordinate System (WCS) to assign a coordinate system to the observed objects. Most of the tasks are automated in the pipeline, although manual intervention is needed for some processing parts. For example, the objects having multiple slices of datasets for a particular band needed to be registered manually with point sources for aligning and merging the images so that translational and/or rotational drifts do not affect the quality of the image. The final calibrated images of our objects from UVIT L1 data are shown in Fig. 2. In this figure, we show the FUV F154W ($\sim 0.1541\mu\text{m}$) observations for all target galaxies and NUV N242W ($\sim 0.2418\mu\text{m}$) observations for the objects NGC 5635 and NGC 266.

In the FUV band, the integration times of the objects NGC 1030, NGC 1961, NGC 4501, NGC 5635 and NGC 266 are $T_{\text{int}} \sim 1.9, 1.9, 1.6, 8.1$ and 7.4 ks, respectively. While, in the NUV band the

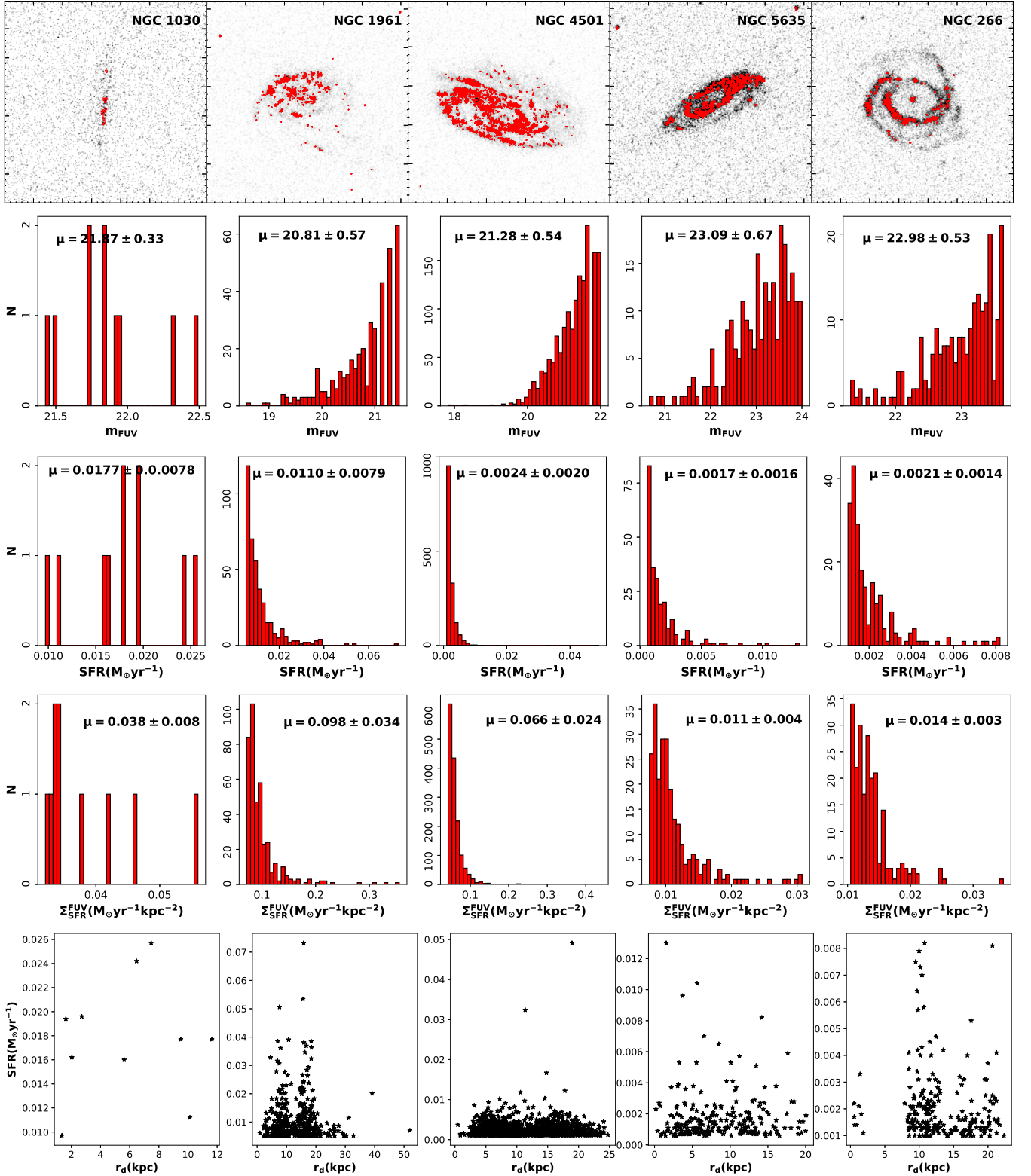


Figure 3. *First row:* Here, we show the young star-forming clumps based on the UVIT far-ultraviolet (FUV) data of the objects that are identified with 3σ detection threshold considering the star-forming clumps to be hierarchical in nature (Robitaille et al. 2019) (Section 3.3). *Second row:* Here, we show the histogram of FUV magnitude (m_{FUV}) of the identified clumps in the AB system for the objects with the mean μ with 1σ uncertainties mentioned in the respective plots. *Third row:* Here, we show the histogram of the FUV star formation rate $SFR(M_{\odot} \text{yr}^{-1})$ of the identified clumps of the objects with mean μ and 1σ uncertainty. *Fourth row:* Here, we show the distribution of FUV star formation rate density $\Sigma_{SFR}^{FUV}(M_{\odot} \text{yr}^{-1} \text{kpc}^{-2})$ of the objects with the mean μ and 1σ uncertainty. *Fifth row:* Here, the variation of the FUV SFR of the identified clumps with radius r_d (kpc) from the centre of the galaxy is shown for each object.

integration times for objects NGC 5635 and NGC 266 are $T_{\text{int}} \sim 8.2, 7.5$ ks, respectively.

3.2 Aperture photometry

We perform aperture photometry of the objects in each band mentioned in Section 2.2. The apertures for finding out the flux of the objects is estimated with the IRAF task *ellipse* (Tody 1986). With the UVIT FUV images as the references, the radius of the aperture is defined as the distance at which the intensity of the source matches the background, which is the mean per pixel calculated from regions away from the source. To estimate the background flux per pixel, we use the SAOImageDS9 task *region* (Joye & Mandel 2003). Depending on the aperture radius, we make image cut-outs for our objects using the IRAF task *incopy*. The data preferences are as follows: (a) for FUV and NUV, we use UVIT for all objects except NGC 1030, NGC 1961 and NGC 4501, where in the absence of UVIT NUV, we use GALEX NUV data, (b) for optical bands we use SDSS for NGC 4501, NGC 5635 and NGC 266. In the absence of SDSS images, we use Pan-STARRS images for NGC 1961 and DECaLS images for NGC 1030; (c) for near-infrared, we use 2MASS for all objects; (d) for mid-infrared, we use WISE for all objects except NGC 4501 due to absence of image covering our entire aperture, and in place of that we use IRAS1 and IRAS2, (e) for far-infrared we use IRAS3 and IRAS4 for all our objects. Note that, in the absence of the entire image in our defined aperture, we have used python module *reproject* to specifically make flux-conserved image mosaics for 2MASS NGC 5635 and 2MASS NGC 266 collecting image frames containing our objects of interest from the corresponding archive. For the same reason, we also use SDSS mosaics, but in this case, we use the SWARP (Bertin et al. 2002; Bertin 2010) script provided by the DR12 Science Archive Server (SAS) to make the mosaics.

To eliminate the contributions from the background sources to the total light within the aperture, we use SExtractor (Bertin & Arnouts 1996) for the image cut-outs with DETECT_THRESH as 3 and subtract their fluxes from the total flux within the defined aperture. To eliminate the effect of overall background contribution, we calculate the background flux per pixel as the mean flux from regions far from any contaminating sources in the images using SAOImageDS9 as mentioned before. The process is carried out for each data mentioned in Section 2.2. Note that, to estimate the fluxes, we use relations provided by Tandon et al. (2017) for UVIT.

Lower wavelength radiations like ultraviolet (UV) light are highly interactive with an interstellar medium consisting of dust grains. The physical dimensions of dust grains are quantified by the power law of Mathis, Rumpl & Nordsieck (1977) to be $\sim 0.005 - 0.25 \mu\text{m}$. Now, with the UV wavelength in the range $\sim 0.01 - 0.4 \mu\text{m}$ it can be susceptible to absorption or scattering by dust grains if the grain size is greater or comparable to the wavelength, respectively. The observed UV light from the star-forming regions of galaxies can be thought to be reprocessed in two steps: internal extinction and foreground galactic extinction. To account for the galactic extinction, we consider the dust map of Schlafly & Finkbeiner (2011) and calculate the band extinctions taking individual reddening and Cardelli et al. (1989) extinction law into consideration. The extinction in a particular wavelength is given by,

$$A_{\lambda} = R_{\lambda}E(B - V) \quad (2)$$

Here, $E(B - V)$ is the color excess for the object. The quantity R_{λ} , the ratio of total to selective total extinction is 3.1 for Milky Way type extinction in V-band (Schultz & Wiemer 1975).

3.3 Star formation hierarchy in the galactic discs

Far-ultraviolet radiations (FUV) from a galaxy are useful tracers of young star-forming populations within the galaxy. FUV can locate the clumps which are hosting star formation in the galaxy over the past ~ 100 Myr. A large star-forming region may contain smaller high-UV-intensity regions with young star formations going on. We consider these star-forming structures to be hierarchical in nature and employ ASTRODENDRO (Robitaille et al. 2019) to identify these regions based on some given constraints. The algorithm of ASTRODENDRO considers an input intensity map (in our case, the UVIT data) to be hierarchical in nature and decompose it like the structure of a tree. The dendrogram is constructed starting with identifying the brightest pixels in the map and progressively adding fainter pixels in the subsequent steps. The dendrogram considered has two types of structures called branches and leaves. A branch can split into another branches and leaves, but leaves do not have any further substructures. All these structures converge into a trunk that has no parent structure (see Robitaille et al. 2019 for more details¹). The large star-forming regions are considered parent structures in ASTRODENDRO, with smaller regions within these as the child structures. We use $\sim (1.8/0.42)$ as the minimum number of pixels based on the resolution and pixel scale of UVIT in order to identify the brightest clumps. The detection threshold for the clumps is set at 3σ level based on the average noise of the data. The young star-forming clumps of the objects identified with 3σ detection threshold are shown in Fig. 3 (First row). The parameters derived from the catalogue of star-forming clumps for the objects are shown in Table 3, and their histograms are shown in the second, third, and fourth rows in Fig. 3. In the same figure, fifth row, the variation of the FUV SFR of the identified clumps with radius r_d (kpc) from the centre of the galaxy is shown for each object.

A cut-out image of a region ($\sim 57 \times 57 \text{ arcsec}^2$) of the star-forming clumps in NGC 1961 is shown in Fig. 4. The green contours indicate the branches and the red contours indicate the child structures or the leaves. It can be seen that many of the leaves are isolated structures showing isolated regions of young star formation. Note that the image pixel values are in the units of $1.87 \times 10^{-18} \text{ erg s}^{-1} \text{ cm}^{-1} \text{ Hz}^{-1}$. The few parameters of the output catalogue of ASTRODENDRO that were made use of are the position coordinates of the clumps, the exact area of the child structures, the flux enclosed by that area, and the effective radius of the clumps. Note that, we have considered the child structures for estimating our parameters as they are more resolved than the parent structures based on the resolution of UVIT.

The star formation rates for the objects are found out following the relation of Kennicutt (1998) between the SFR and far-ultraviolet luminosity L_{FUV} assuming a Salpeter Initial Mass Function (IMF) with mass limits $0.1 - 100 M_{\odot}$ which is given below,

$$\text{SFR}_{\text{FUV}}(M_{\odot}\text{yr}^{-1}) = 1.4 \times 10^{-28} L_{\text{FUV}}(\text{erg s}^{-1}\text{Hz}^{-1}) \quad (3)$$

Note that, we estimate all the SFRs in this paper considering a Salpeter initial mass function (IMF). The magnitude m_{FUV} , SFR and $\Sigma_{\text{SFR}}^{\text{FUV}}$ mentioned in Table 3 are corrected for both foreground and internal attenuation of the galaxies. To estimate the corrected magnitude and/or flux of the clumps, the effect of foreground attenuation of radiation is taken into account following the procedure described in Section 3.2 and to eliminate the effect of the internal attenuation within the host galaxies in FUV wavelength, we consider the total extinction A_{FUV} (mag) found out from the best-fit spectral

¹ <https://dendrograms.readthedocs.io/en/stable/>

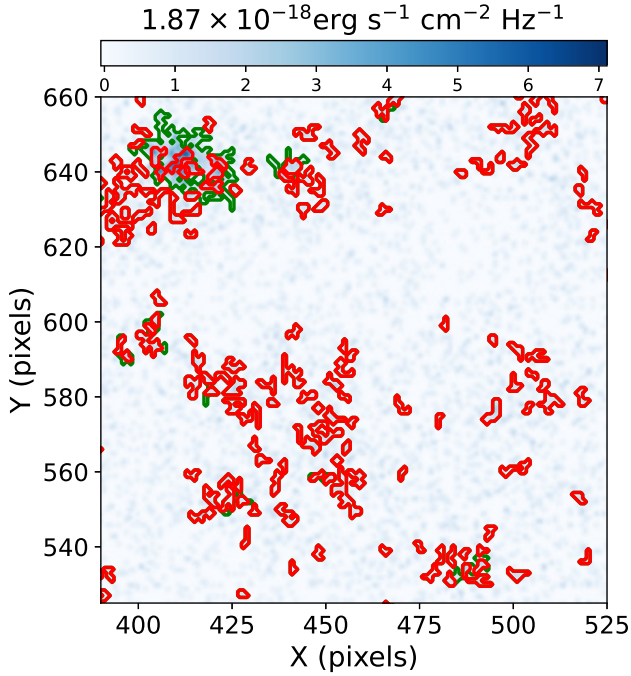


Figure 4. Here, we show a cut-out region ($\sim 57 \times 57$ arcsec 2) of star forming clumps (Fig. 3) of the object NGC 1961. The green contours indicate the branches and the red contours indicate the child structures or the leaves. It can be seen that many of the leaves are isolated structures showing isolated regions of young star formation. Note that the image pixel values are in the units of $1.87 \times 10^{-18} \text{erg s}^{-1} \text{cm}^{-2} \text{Hz}^{-1}$.

Parameters	NGC 1030	NGC 1961	NGC 4501	NGC 5635	NGC 266
N	10	393	1511	238	219
m_{FUV}	21.87	20.81	21.28	23.09	22.98
	± 0.33	± 0.57	± 0.54	± 0.67	± 0.53
SFR	0.0177	0.0110	0.0024	0.0017	0.0021
	± 0.0078	± 0.0079	± 0.0020	± 0.0016	± 0.0014
$\Sigma_{\text{SFR}}^{\text{FUV}}$	0.038	0.098	0.066	0.011	0.014
	± 0.008	± 0.034	± 0.024	± 0.004	± 0.003
r_{eff}	160-317	57-251	34-168	69-310	72-270

Table 3. In the above table, we mention the mean (μ) and 1σ uncertainty of the parameters derived from the catalogue of star-forming clumps of the objects identified with 3σ detection threshold in ASTRODENDRO (Robitaille et al. 2019). The parameters are described below N = the number of clumps, m_{FUV} = magnitude of the identified clumps in the AB system, SFR = star formation rate of the identified clumps in $M_{\odot} \text{yr}^{-1}$, $\Sigma_{\text{SFR}}^{\text{FUV}}$ = star formation rate density of the clumps in $M_{\odot} \text{yr}^{-1} \text{kpc}^{-2}$, r_{eff} = effective radius (min value-max value) of the star-forming clumps in pc. All the parameters are derived for the area within the apertures mentioned in Table 2. Note that m_{FUV} , SFR and $\Sigma_{\text{SFR}}^{\text{FUV}}$ shown here are corrected for foreground and internal dust attenuation.

energy distribution of the objects using the grid shown in Table 4 and are mentioned in Table 5 (see Section 3.4 for details).

3.4 The Spectral Energy Distribution

To fit the spectral energy distribution (SED) of the objects, we have made use of data from our UVIT observations as well as other archival data for our objects as mentioned in Section 2.2. The steps followed

to estimate the fluxes in FUV-FIR bands of the objects are given in Section 3.2. We used CIGALE (v2022) (Code Investigating GALaxy Emission) (Boquien et al. 2019; Yang et al. 2022) to perform SED fitting, where we utilized multi-band photometry data of the objects given as inputs. The FUV-FIR fluxes are corrected for attenuation due to foreground dust before using them as inputs to CIGALE. The modules used to perform the fitting are described below,

(i) Star formation history: The module *sfdelayed* is used to model the star formation history of the objects. Here, the star formation model is defined as $\text{SFR}(t) \propto \frac{1}{\tau^2} \exp(-t/\tau)$ for t as the variable of time and where τ defines the peak of the star-forming history of a galaxy.

(ii) Stellar populations: The module *bc03* is used to model the stellar population of the galaxies (Bruzual & Charlot 2003).

(iii) Nebular emission: The module *nebular* is used to fit the nebular emission (Inoue 2011) in galaxies beyond mid-infrared as a result of heating and ionisation of gas surrounding massive stars, which denotes young star-forming regions within the galaxy.

(iv) Dust attenuation: The module *dustatt_calzleit* is used to model the attenuation of light in the galaxy. The dust absorbs radiation in shorter wavelengths (ultraviolet and near-infrared) and re-radiates them in mid and far-infrared. Here we use models as per Calzetti et al. (2000) to account for the attenuation.

(v) Dust emission: We use *dl2014* to fit the re-processed radiation in mid and far-infrared and beyond (Draine et al. 2014).

(vi) AGN: To account for the effect of the active galactic nuclei (AGN) in the overall SED, we make use of *fritz2006* as per Fritz et al. (2006).

We have fitted the spectral energy distribution of each object in our sample individually. The CIGALE grid used to find out the best-fit SEDs for the objects is described in Table 4, where we mention all the free parameters related to the models described above have been used to optimize the fittings. The final best-fit model SEDs for the objects and the observed multi-band photometric data points used as inputs are shown in graphs in Fig. 5. This figure shows CIGALE's best-fit models of the objects' spectral energy distributions. The data points are shown with empty black circles, and the models are shown with black lines. In the lower parts of each graphs, we show the filled transmission curves for the bands used for wavelength references. Filters from left to right: UVIT F154W, UVIT N242W, SDSS u, SDSS g, SDSS r, SDSS i, SDSS z, WISE1, WISE2, WISE, WISE4, IRAS60, IRAS100. Note that we have also made use of DECaLS (g, r, z) and Pan-STARRS1 (g, r, i, z, y) images for NGC 1030 and NGC 1961 respectively (Section 2.2).

As mentioned earlier, the free parameters for the fitting are shown in Table. 4 and it is important to note that, we have fitted each of the galaxies individually instead of a batch fitting in order to observe the variations of the parameters more carefully for each galaxies and change them accordingly to optimize the fitting though minimization of reduced chi-square (χ^2_{ν}). At first, for each of our objects we start the fitting by the default script generated by CIGALE and then change the free parameters individually and take into account different combinations of them in order to obtain a better fit for each galaxies. This can be noted from the different set of choices for a single parameter (e.g. τ_{main}) in case of different galaxies. The free parameters corresponding to the modules described before in this section and also mentioned in the Table. 4 are described as the following: (i) star formation history is parameterized by e-folding time of the main stellar population model (τ_{main}), age of the main stellar population in the galaxy (Age), e-folding time of the late starburst population model (τ_{burst}), age of the late burst (Age $_{\text{burst}}$) and mass

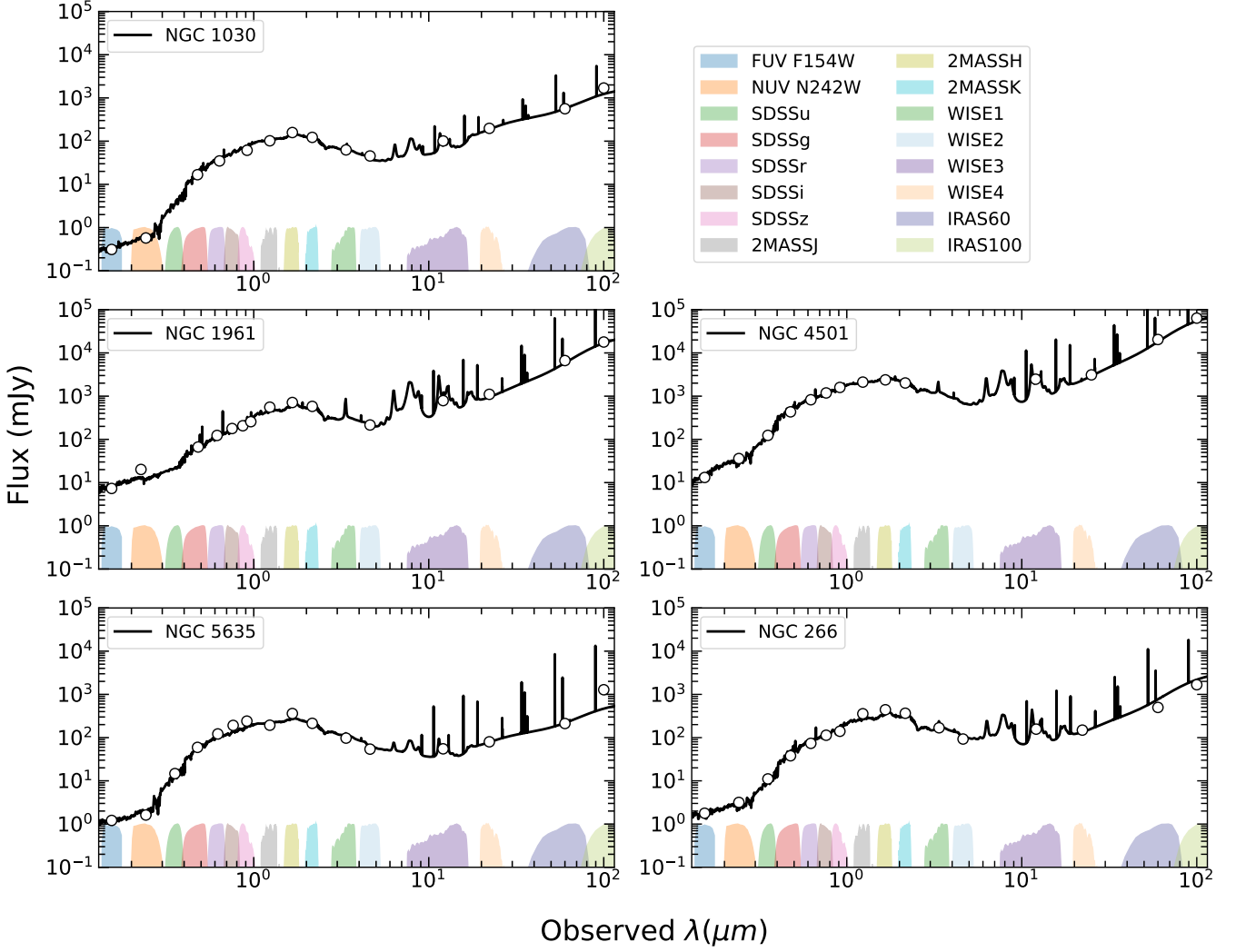


Figure 5. The best-fit models of the spectral energy distributions of the objects using CIGALE are shown. The data points are shown with empty black circles, and the models are shown with black lines. We have employed the following modules to estimate the best-fit results from the FUV-FIR SED: *sfdelayed* for star formation history SFH, *bc03* for a single stellar population SSP, *nebular* for nebular emission lines, *dustatt_calzleit* for dust attenuation, *dl2014* for dust emission, *fritz2006* for AGN contribution. In the lower part of each graph, we show the bands that have been used to find the SEDs of the objects. Filters from left to right: F154W, N242W, SDSS u, SDSS g, SDSS r, SDSS i, SDSS z, 2MASS J, 2MASS H, 2MASS K, WISE1, WISE2, WISE3, WISE4, IRAS60, IRAS100. The filters with their corresponding colors are also shown in the top right corner of the figure. Note that we have also made use of DECaLS (g, r, i, z, y) and Pan-STARRS1 (g, r, i, z, y) images for NGC 1030 and NGC 1961 respectively (Section 2.2).

fraction of the late burst population (f_{burst}), (ii) Stellar population is parameterized by the initial mass function (IMF), metallicity, (iii) dust attenuation is parameterized by colour excess of the stellar continuum light for the young population ($E(B - V)_{\text{young}}$), Reduction factor for the $E(B - V)$ of the old population compared to the young one ($E(B - V)_{\text{old-factor}}$), (iv) dust emission is parameterized by mass fraction of Polycyclic Aromatic Hydrocarbon PAH (q_{PAH}), power-law slope α for $\frac{dU}{dM} \propto U^\alpha$. Note that, here, we only mention the parameters that have been varied during the fitting (for more details on each module, see Boquien et al. 2019).

The results of the SED fitting are tabulated in the upper panel of Table 5. We mention the best-fit outputs of some of the parameters of our interest and their parent modules: (i) *sfdelayed*: instantaneous star formation rate $\text{SFR}_{\text{inst}} (M_\odot \text{yr}^{-1})$, e-folding time of the main stellar population model $\tau_{\text{main}} (\text{Gyr})$, (ii) *bc03*: total stellar mass $M_\star (M_\odot)$, stellar mass of the young population $M_{\star, \text{young}} (M_\odot)$,

total stellar luminosity $L_\star (L_\odot)$, (iii) *dustatt_calzleit*: attenuation in UVIT FUV wavelength $A_{\text{FUV}} (\text{mag})$, (iv) *dl2014*: dust mass $M_{\text{dust}} (M_\odot)$, dust luminosity $L_{\text{dust}} (L_\odot)$. Note that, in our best-fit SEDs of the objects, we found negligible/ almost no contribution from the AGN, indicating at the present day not much activity is taking place in the galactic nuclei of these massive spirals. In the lower panel of Table 5, we show some more parameters estimated using SED-derived data and other parameters shown in Table 2. We estimate the old to young stellar population ratio ζ from SED, where we find the mass of the older stellar population $M_{\star, \text{old}} \sim M_\star$. The stellar mass accumulated up to the peak of the star-forming activity (denoted by τ_{main}) of the corresponding objects are denoted by $M_{\star, \text{peak}} (M_\odot)$. The total baryonic mass $M_{\text{baryon}} (M_\odot)$ of these galaxies are estimated using the stellar mass M_\star , dust mass M_{dust} (both shown in upper panel, Table 5) and gas mass M_{gas} (Table 2). The expected baryonic mass these spirals should have as per the mean cosmological baryon

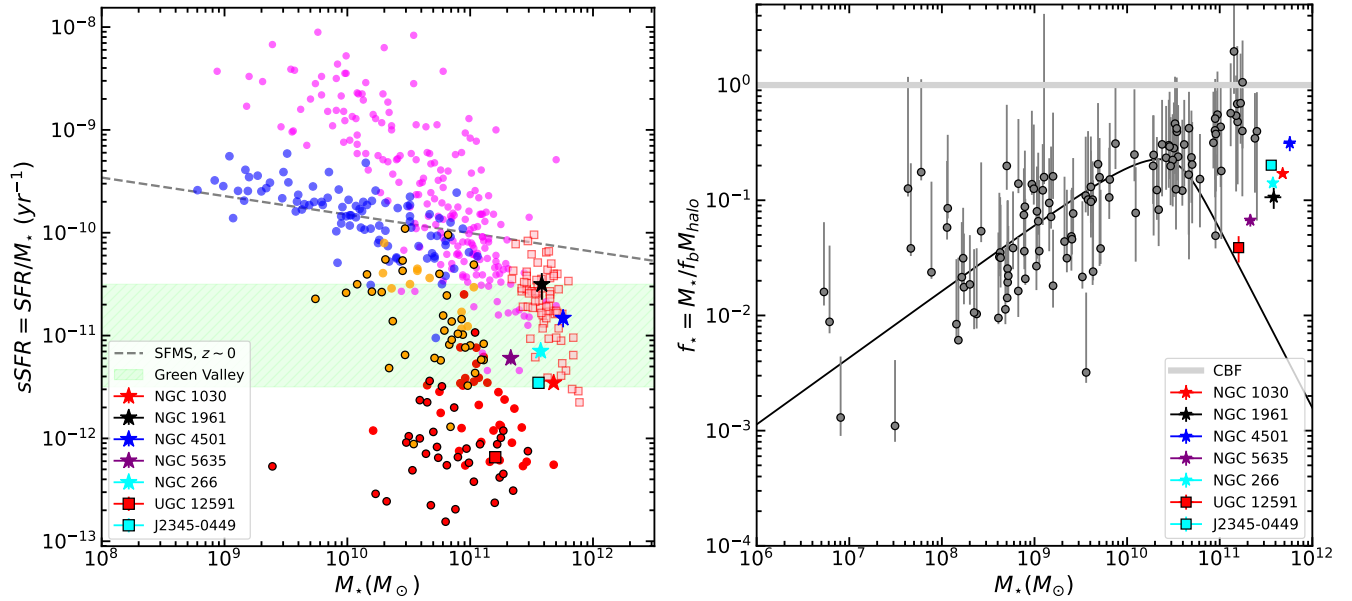


Figure 6. *Left panel:* Variation of specific star formation rate (sSFR in yr^{-1}) versus the stellar mass (M_* in M_\odot) is shown for galaxies of various types. The dotted line indicates the star-forming main sequence from $z \sim 0$ (Elbaz et al. 2007). Highly Star-forming ultraviolet luminous galaxies are taken from Hoopes et al. (2007) (filled magenta circles). Super spirals, lenticulars and post-merger galaxies from Ogle et al. (2019a) (orange boxes with red edges). A sample of galaxies with different quenching stages like the star-forming (filled blue circles), mixed (filled orange circles with black edges), nearly retired (filled red circles), fully retired (filled red circles with black edges) and quiescent-nuclear-ring (filled orange circles) taken from Kalinova et al. (2021) are also shown. The positions of five target galaxies from the present study are shown with star symbols, with instantaneous SFR and stellar mass from SED using CIGALE. The light green shadow indicates the green valley region with $10^{-11.5} < \text{sSFR} < 10^{-10.5}$ (Salim et al. 2016). *Right panel* shows the variation of the star formation efficiency f_* of the galaxies as a function of its stellar mass M_* . The black curve is obtained from the relation between halo mass and the corresponding stellar mass provided by Moster et al. (2013) using a multi-epoch abundance matching model. Here, we show the model for redshift $z \sim 0$. The SPARC (Spitzer Photometry and Accurate Rotation Curves) sample of disc galaxies (Lelli et al. 2016; Posti et al. 2019) is shown with black+grey points. In the case of $M_*/M_{\text{halo}} = f_b$, cosmic baryon fraction (CBF), the star formation efficiency $f_* = 1$ and is shown with the light grey line.

Modules	Parameters	Units	NGC 1030	NGC 1961	NGC 4501	NGC 5635	NGC 266
Star formation history: (<i>sfhdelayed</i>)	(a) τ_{main}	Myr	1–8000;20	500–5000;5	1–5000;20	1–8000;20	1000–13000;13
	(b) Age	Myr	1000–13000;13	1000–13000;13	500–13000;8	5000–13000;20	5000–13000;8
	(c) τ_{burst}	Myr	[5,10,25, 50,100]	[1,5,10, 25,50,100]	[5, 10, 25, 50, 100]	[1, 5, 10, 25, 50, 100]	[5, 10, 25, 50, 100]
	(d) $\text{Age}_{\text{burst}}$	Myr	[5, 10, 25, 50, 100, 200, 350, 500, 750, 1000]	[5,10,25, 50,100,200, 350,500,750, 1000]	[5, 10, 25, 50, 100, 200, 350, 500, 750, 1000]	[50, 100, 200, 350, 500, 750, 1000,1250, 1500]	[5, 10, 25, 50, 100, 200, 350, 500, 750, 1000]
	(e) f_{burst}	–	[0, 0.0001, 0.0005, 0.001, 0.005, 0.01, 0.05, 0.1, 0.25]	[0, 0.0001, 0.0005, 0.001, 0.005, 0.01, 0.05]	[0, 0.0001, 0.0005, 0.001, 0.005, 0.01, 0.05, 0.1, 0.25]	[0.0001, 0.0005, 0.001, 0.005, 0.01, 0.05, 0.1, 0.25]	[0, 0.0001, 0.0005, 0.001, 0.005, 0.01, 0.05, 0.1, 0.25]
Stellar population: (<i>bc03</i>)	(f) IMF	–	Salpeter	Salpeter	Salpeter	Salpeter	Salpeter
	(g) Metallicity	–	0.02, 0.05	0.02, 0.05	0.02, 0.05	0.02, 0.05	0.02, 0.05
Dust attenuation: (<i>dustatt_calzleit</i>)	(h) $E(B - V)_{\text{young}}$	–	0.1–1;5	0–3;15	0–3;15	0–3;15	0–1;10
	(i) $E(B - V)_{\text{old-factor}}$	–	0.5–1;4	0–1;10	0–1;10	0–1;10	0.1–1;10
Dust emission: (<i>dl2014</i>)	(j) q_{PAH}	–	2.5	6.63	3.90	3.90	7.32
	(k) α	–	2.0	2.2	2.2	2.0	2.2

Table 4. Here, we mention the grid used in CIGALE to find out the best-fit parameters. The parameters are as follows: (a) τ_{main} = E-folding time of the main stellar population model, (b) Age = Age of the main stellar population in the galaxy, (c) τ_{burst} = E-folding time of the late starburst population model, (d) $\text{Age}_{\text{burst}}$ = Age of the late burst, (e) f_{burst} = Mass fraction of the late burst population, (f) IMF = Initial Mass Function (Salpeter; Salpeter 1955), (g) Metallicity, (h) $E(B - V)_{\text{young}}$ = Colour excess of the stellar continuum light for the young population, (i) $E(B - V)_{\text{old-factor}}$ = Reduction factor for the $E(B - V)$ of the old population compared to the young one, (j) q_{PAH} = Mass fraction of PAH, (k) α = Power-law slope for $\frac{dU}{dM} \propto U^\alpha$. Note that $\tau_{\text{main}} = 1 - 8000; 20$ means that τ_{main} is varied between 1 and 8000 with 20 evenly spaced values as inputs. And also, the parameters for which one single value (e.g. q_{PAH} , α) is mentioned, that is, the best fit value for that parameter obtained through multiple iterations.

Parameters	Units	NGC 1030	NGC 1961	NGC 4501	NGC 5635	NGC 266
SFR_{inst}	$M_{\odot}\text{yr}^{-1}$	1.66 ± 0.08	12.04 ± 2.48	8.45 ± 0.97	1.29 ± 0.06	2.65 ± 0.27
M_{\star}	M_{\odot}	$(4.78 \pm 0.24) \times 10^{11}$	$(3.83 \pm 0.79) \times 10^{11}$	$(5.71 \pm 0.85) \times 10^{11}$	$(2.14 \pm 0.27) \times 10^{11}$	$(3.75 \pm 0.33) \times 10^{11}$
$M_{\star,\text{young}}$	M_{\odot}	$(1.62 \pm 0.08) \times 10^7$	$(1.27 \pm 0.21) \times 10^8$	$(8.21 \pm 0.95) \times 10^7$	$(1.26 \pm 0.06) \times 10^7$	$(2.55 \pm 0.26) \times 10^7$
M_{dust}	M_{\odot}	$(1.29 \pm 0.06) \times 10^8$	$(4.87 \pm 0.27) \times 10^8$	$(4.04 \pm 0.25) \times 10^8$	$(1.33 \pm 0.07) \times 10^7$	$(8.85 \pm 0.44) \times 10^7$
L_{\star}	L_{\odot}	$(2.54 \pm 0.13) \times 10^{11}$	$(2.96 \pm 0.15) \times 10^{11}$	$(4.04 \pm 0.20) \times 10^{11}$	$(1.22 \pm 0.06) \times 10^{11}$	$(1.67 \pm 0.08) \times 10^{11}$
L_{dust}	L_{\odot}	$(4.72 \pm 0.24) \times 10^{10}$	$(1.15 \pm 0.06) \times 10^{11}$	$(1.05 \pm 0.05) \times 10^{11}$	$(4.83 \pm 0.24) \times 10^9$	$(2.16 \pm 0.11) \times 10^{10}$
A_{FUV}	mag	1.017 ± 0.003	1.734 ± 0.125	1.632 ± 0.034	0.857 ± 0.003	0.865 ± 0.011
τ_{main}	Gyr	0.843	2.750	2.106	0.843	2.000
χ^2_{ν}	–	1.20	2.40	0.81	4.00	2.30
ζ	–	$(2.95 \pm 0.21) \times 10^4$	$(3.02 \pm 0.80) \times 10^3$	$(6.95 \pm 1.31) \times 10^3$	$(1.70 \pm 0.23) \times 10^4$	$(1.47 \pm 0.20) \times 10^4$
$M_{\star,\text{peak}}$	M_{\odot}	1.73×10^{11} (36.19%)	1.62×10^{11} (42.30%)	2.30×10^{11} (40.28%)	0.66×10^{11} (30.84%)	1.25×10^{11} (33.33%)
M_{baryon}	M_{\odot}	$(5.10 \pm 0.24) \times 10^{11}$	$(5.41 \pm 0.85) \times 10^{11}$	$(5.99 \pm 0.85) \times 10^{11}$	$(2.63 \pm 0.27) \times 10^{11}$	$(4.11 \pm 0.34) \times 10^{11}$
M_{expected}	M_{\odot}	2.81×10^{12}	3.61×10^{12}	1.82×10^{12}	3.19×10^{12}	2.66×10^{12}
$f_{\text{b},r200}$	–	0.030 ± 0.001	0.025 ± 0.004	0.055 ± 0.008	0.014 ± 0.001	0.026 ± 0.002
f_{\star}	–	0.170 ± 0.009	0.106 ± 0.022	0.314 ± 0.047	0.067 ± 0.008	0.141 ± 0.012

Table 5. Here, in the upper panel of the table, we mention the best-fit output parameters for SED fitting in CIGALE. The mentioned parameters are as follows: SFR_{inst} = instantaneous star formation rate, M_{\star} = stellar mass, $M_{\star,\text{young}}$ = mass of young stellar population, M_{dust} = dust mass, L_{\star} = stellar luminosity, L_{dust} = dust luminosity, A_{FUV} = extinction in F154W FUV-band of UVIT, τ_{main} = the peak age of star formation of the main stellar population of the objects, χ^2_{ν} = reduced chi-square of the best fit. In the lower panel, we mention some more useful parameters calculated using SED-derived data. We show, $\zeta = M_{\star,\text{old}}/M_{\star,\text{young}}$ = the ratio of the stellar mass of old to young population, $M_{\star,\text{peak}}$ = stellar mass of the objects accumulated by time τ_{main} with the percentage of the present day stellar mass M_{\star} in bracket, $M_{\text{baryon}} = M_{\star} + M_{\text{gas}} + M_{\text{dust}}$ = total baryonic mass (see Table 2 for M_{gas}), M_{expected} = baryonic mass of the galaxies expected from the cosmic baryon fraction of 0.167 and the halo mass M_{halo} (see Table 2), $f_{\text{b},r200} = M_{\text{baryon}}/M_{\text{halo}}$ = baryon fraction of the galaxies taking total baryonic mass and the halo mass upto the virial radius and, $f_{\star} = M_{\star}/f_{\text{b}}M_{\text{halo}}$ = star formation efficiency.

fraction is shown by $M_{\text{expected}} = f_{\text{b}}M_{\text{halo}}$, where $f_{\text{b}} = 0.167$ and the halo mass M_{halo} is shown in Table 2. However, the baryon fraction that is seen in these galaxies within the virial radius r_{200} is denoted by $f_{\text{b},r200}$ as the ratio of M_{baryon} to M_{halo} . Finally, we mention the star formation efficiency of these objects, which is denoted by $f_{\star} = M_{\star}/f_{\text{b}}M_{\text{halo}}$, which characterises the efficiency of halo baryons' conversion into stars. It can be seen that all of our spirals have stellar mass $> 10^{11}M_{\odot}$ (and luminosity $> 10^{11}L_{\odot}$) comparable to high-mass elliptical galaxies. The instantaneous star formation rate of these objects falls in between $1.29 - 12.04M_{\odot}\text{yr}^{-1}$ considering a delayed star formation history model (Section 3.4), where the peak star formation of these objects happened in between $0.843 - 2.750$ Gyr after the 'Big Bang'.

The star formation rates of the objects as a function of the stellar mass is shown in (Fig. 6, left panel). In this figure, the variation of specific star formation rate (sSFR in yr^{-1}) versus the stellar mass (M_{\star} in M_{\odot}) is shown for galaxies of various types. The dotted line indicates the star-forming the main sequence from $z \sim 0$ (Elbaz et al. 2007). Highly Star-forming ultraviolet luminous galaxies are taken from Hoopes et al. (2007) (filled magenta circles). Super spirals, lenticulars and post-merger galaxies are taken from Ogle et al. (2019a) (orange boxes with red edges). A sample of galaxies with different quenching stages like the star-forming (filled blue circles), mixed (filled orange circles with black edges), nearly retired (filled red circles), fully retired (filled red circles with black edges) and quiescent-nuclear-ring (filled orange circles) taken from Kalinova et al. (2021) have also been shown. The positions of the five target galaxies of the present study are shown with star symbols, with instantaneous SFRs and stellar masses given in Table 5. Despite their high stellar masses, one can see that their sSFR is anomalously low, much below the main sequence, and close to the region of the most massive super spirals of Ogle et al. (2019a), but above the highly quenched, fully retired galaxies. The 'Green Valley' region with $10^{-11.5} < \text{sSFR}(\text{yr}^{-1}) < 10^{-10.5}$ (Salim et al. 2016) is shown with light green shadow.

Moreover, we also show the variation of the star formation effi-

ciency f_{\star} of the galaxies as a function of its stellar mass M_{\star} in (Fig. 6, right panel). Using a multi-epoch abundance matching model, the black curve is obtained from the relation between halo mass and the corresponding stellar mass provided by Moster et al. (2013). The SPARC (Spitzer Photometry and Accurate Rotation Curves) sample of disc galaxies (Lelli et al. 2016; Posti et al. 2019) is shown with black+grey points. In the case of $M_{\star}/M_{\text{halo}} = f_{\text{b}}$, cosmic baryon fraction (CBF), the star formation efficiency $f_{\star} = 1$ and is shown with the light grey line.

4 DISCUSSION

4.1 Star formation

The ultraviolet radiation from the young star-forming regions of a galaxy gets absorbed by the dust in the interstellar medium (ISM) and ultimately re-emitted in the thermal infrared. Kennicutt (1998) shows that the far-infrared luminosity integrated over $8 - 1000\mu\text{m}$ is a sensitive tracer of young star formation in a galaxy. Now, to account for the absorbed FUV radiation by the dust in the ISM, we use the relation provided by Kennicutt & Evans (2012) and estimate the corrected FUV luminosity using the following relation,

$$L_{\text{FUV}}^{\text{corr}} = L_{\text{FUV}}^{\text{obs}} + 0.46L_{\text{TIR}} \quad (4)$$

Here, $L_{\text{FUV}}^{\text{corr}}$ and $L_{\text{FUV}}^{\text{obs}}$ are the dust corrected and observed luminosity in far-ultraviolet, L_{TIR} = total infrared luminosity over $8 - 1000\mu\text{m}$. We use the observed luminosity $L_{\text{FUV}}^{\text{obs}}$ of the objects as per the foreground extinction corrected magnitudes mentioned in Table 2. The integrated luminosity is estimated as, $L_{\text{TIR}} \sim 1.75L_{\text{FIR}}$ (Calzetti et al. 2000), where the far-infrared luminosity L_{FIR} is found out using IRAS 60 and $100\mu\text{m}$ fluxes following Helou et al. (1988). The star formation rates of the objects using the dust-corrected FUV luminosities are shown in Table 2 as $SFR_{\text{FUV}}^{\text{corr}}(M_{\odot}\text{yr}^{-1})$. The spirals NGC 1961 and NGC 4501 have the highest FUV star formation

of 13.66 and $13.51 M_{\odot} \text{yr}^{-1}$ respectively followed by NGC 1030, NGC 266 and NGC 5635.

Massive galaxies often show a quenched state of star formation at low red-shift. The general idea has been that they acquire most of their mass earlier in time compared to the main-sequence galaxies. In Fig. 6 (left panel), we show the variation of the specific star formation rates of the galaxies as a function of their stellar masses for a wide range of samples, including galaxies at different stages of their evolution and properties where we mention ultraviolet luminous galaxies from Hoopes et al. (2007), the super spiral, lenticular and post-merger galaxies from Ogle et al. (2019b) and a mixed group of star-forming, nearly retired and fully retired galaxies from Kalinova et al. (2021). It can be seen that our sample galaxies with stellar mass $\gtrsim 10^{11} M_{\odot}$ fall below the expectation of the main-sequence relation at $z \sim 0$ (Elbaz et al. 2007), specifically in the ‘Green Valley’ region with specific star formation rates in $10^{-11.5} < \text{sSFR} < 10^{-10.5} \text{yr}^{-1}$ (Salim et al. 2016), confirming the overall trend of lower star formation with increasing stellar mass which is evident from the graph (see Table 5 for M_{\star} and instantaneous SFR). Even if we consider the specific star formation rates of our objects using FUV dust-corrected star formation rates and their K-band stellar masses (see Table 2 for $\text{sSFR}_{\text{FUV}}^{\text{corr}} (\text{yr}^{-1})$), they fall in the ‘Green Valley’ region indicating they have been in this state for at least the last $\sim 100 \text{Myr}$ considering FUV radiation is indicative of star formation in a galaxy in the past $\sim 100 \text{Myr}$ (Kennicutt & Evans 2012). The intermediate spiral NGC 1961, which has the highest star formation in our sample, is the closest to the main-sequence relation, followed by NGC 4501. NGC 1030 shows the lowest instantaneous SFR, falling almost at the same place as J2345-0449, which is a spiral galaxy hosting a large-scale radio jet (Bagchi et al. 2014). However, our sample of late-type spirals shows a mix of moderate and/or nearly retired instantaneous star formation as opposed to a fully quenched state as shown by the massive isolated S0-a galaxy UGC 12591 (Ray et al. 2022).

In Table 5 (upper panel), we mention the best-fit τ_{main} for the objects, which indicates the peak of star formation activity in the galaxies according to a delayed SFR function as described in Section 3.4. Based on our assumed star formation history, we find that all the objects barring NGC 1961 had experienced a peak in their star formation before the peak in the cosmic star formation history, the ‘cosmic noon’ around $1 < z < 3$ translating to a period of $\sim 2.2 - 5.9$ Gyr after the ‘Big Bang’. We also show that the objects already became massive by the time τ_{main} and gained stellar mass $M_{\star, \text{peak}}$ of the order of a *few* $\times 10^{11} M_{\odot}$ before and up to the peak of their star formation histories, corresponding to a growth of $\sim 31 - 42$ per cent in a time $(1/16) - (1/5)^{\text{th}}$ of the age of the Universe (Table 5). According to our model, the objects that had experienced the peak relatively sooner after the ‘Big Bang’ show a more suppressed state of star formation in recent times (e.g. NGC 1030, NGC 5635, NGC 266) compared to the objects that had their peak relatively in the later period (e.g. NGC 1961, NGC 4501) are still forming stars (Table 2 and 5).

From the spectral energy distribution of these late-type spirals, we also found the contribution of the older stellar population and the younger stellar population in determining the total stellar mass of these objects. We mention the stellar mass of young population $M_{\star, \text{young}}$ in Table 5 (upper panel), and it can be seen that these are much smaller than the total stellar mass of the objects, i.e. $M_{\star, \text{young}} \ll M_{\star}$. However, NGC 1961 and NGC 4501, having the highest young star formations among the five objects, have ~ 10 times more young stellar populations than the other three spirals. We find that these massive galaxies are dominated by older stars, as can be seen from the ratio ζ between old and young stellar mass

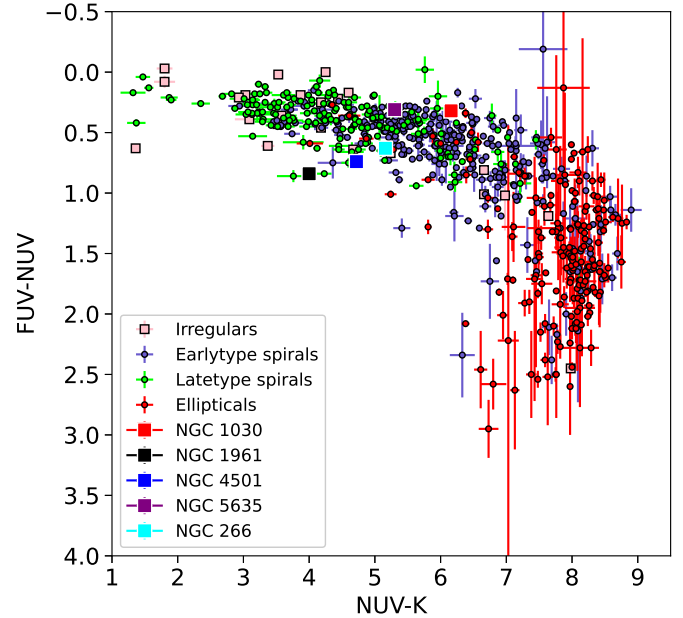


Figure 7. Here, we show the color-color diagram taking foreground extinction corrected (FUV-NUV) and (NUV-K) colors into account from the GALEX ultraviolet ATLAS of nearby galaxies (Gil de Paz et al. 2007). We plot our objects with galaxies of wide morphologies ranging from ellipticals (red) to late-type spirals (green).

in Table 5 (lower panel) with $M_{\star, \text{old}} \sim M_{\star}$. This is also evident from the fact that for our objects K-band stellar mass $M_{\text{K}} \sim M_{\star}$ (see Table 2, Section 4.3), considering K-band luminosity of a galaxy is primarily dominated by radiations from the galaxy’s older stellar population. And objects having a higher population of older stars relative to young stars (hence higher value for ζ) show lower τ_{main} (Table 5) as their main stellar population had peaked sooner after the ‘Big Bang’. This is also visible from the graph in Fig. 7, where we show foreground extinction corrected color-color diagram (considering FUV-NUV and NUV-K colors) for elliptical, spiral and irregular galaxies in the nearby Universe from Gil de Paz et al. (2007). In that graph, we find the color NUV-K for our objects increases as τ_{main} decreases indicating a relatively more older stellar population in objects with smaller τ_{main} , evident from our discussion about ζ and τ_{main} (Table 5). Now, as per the hierarchical structure formation theory of the standard ΛCDM cosmology, where it is assumed that massive systems like these galaxies are formed through the merger of smaller objects over some time, so, they must have more young stellar population instead of older stellar population. The lack of understanding of this well-known problem related to this aspect of galaxy formation theory has also been reported by Man & Belli (2018), Thomas et al. (2005, 2010). One possible solution to that problem could be that these massive galaxies are formed through merging with relatively more minor objects with their own rapid ‘in situ’ star formations that occurred in the early universe, and the merged system undergoes negligible new star formation in the later period of evolution as suggested by Oser et al. (2010). However, careful investigation of the high redshift galaxies, more rigorous parameterization of the star formation histories, and detailed understanding of the baryonic processes in the dark matter halos are some of the key aspects to exactly establish and perhaps solve the problem.

However, the recent periods ($\sim 100 \text{Myr}$) of star formation seen

predominantly in NGC 1961 and NGC 4501 are most probably due to some recent interaction(s) that caused asymmetries in the galactic plane, clearly visible in NGC 1961 optical image as we discussed in Section 2.1. Even though there are no signatures of recent head-on mergers in our objects, the turbulence in the galactic disc provided by strong interaction(s) can make it susceptible to new star formations (Bournaud 2011). In Section 2.1, we mention that all our objects show a varying order of asymmetry and/or interaction, which has helped them to revive star formation to some degree, unlike the quenched disc galaxy UGC 12591 (Ray et al. 2022) situated in an isolated environment devoid of any interaction. However, the exact mechanism of the process is contested (Pearson et al. 2019) and may vary if subjected to morphologically different galaxies and the environment they reside in. Our results are in parallel to the findings of Xu et al. (2020) who show that although the massive galaxies are mostly quiescent in nature, there exists a fraction (~ 20 per cent) of them that are forming stars and of them, ~ 85 per cent have asymmetries induced in their structures by recent mergers.

4.2 Star forming clumps

The UVIT far-ultraviolet images have been spatially resolved into hierarchical star-forming clumps and are shown in Fig. 3 (First row). We show the statistics of the identified clumps in the consequent rows of Fig. 3. We find the least number of structures in NGC 1030 (Table 3) corresponding to very few regions of ongoing star formation with a radius ranging between 160–317 pc partly due to the edge-on view and the existence of dust lanes as can be seen from the optical image Fig. 1. The identified clumps vary over a magnitude of ~ 1 -mag showing similar star-formation going on in them with mean star formation rate (SFR) of $0.0177 \pm 0.0078 M_{\odot} \text{yr}^{-1}$ and mean star formation rate density ($\Sigma_{\text{SFR}}^{\text{FUV}}$) of $0.038 \pm 0.008 M_{\odot} \text{yr}^{-1} \text{kpc}^{-2}$. In NGC 1961 we find 393 clumps (Table 3) with magnitude varying over ~ 3 -mag and having the highest SFR and $\Sigma_{\text{SFR}}^{\text{FUV}}$ with mean value of $0.0110 \pm 0.0079 M_{\odot} \text{yr}^{-1}$ and $0.098 \pm 0.034 M_{\odot} \text{yr}^{-1} \text{kpc}^{-2}$ respectively. Even though the dust-corrected FUV SFR is similar for NGC 1961 and NGC 4501 (Table 2), their clumps statistics differ significantly. NGC 4501 has the highest number of star-forming clumps, with 1511 clumps having a radius between 34–168 pc and mean SFR and $\Sigma_{\text{SFR}}^{\text{FUV}}$ of $0.0024 \pm 0.0020 M_{\odot} \text{yr}^{-1}$ and $0.066 \pm 0.024 M_{\odot} \text{yr}^{-1} \text{kpc}^{-2}$ respectively. The clumps of the object NGC 266 show lower mean SFR and $\Sigma_{\text{SFR}}^{\text{FUV}}$ of $0.0021 \pm 0.0014 M_{\odot} \text{yr}^{-1}$ and $0.014 \pm 0.003 M_{\odot} \text{yr}^{-1} \text{kpc}^{-2}$ respectively followed by NGC 5635 with the parameters as $0.0017 \pm 0.0016 M_{\odot} \text{yr}^{-1}$ and $0.011 \pm 0.004 M_{\odot} \text{yr}^{-1} \text{kpc}^{-2}$ respectively. It can be seen that the mean local dust corrected magnitude m_{AB} and star formation rate density $\Sigma_{\text{SFR}}^{\text{FUV}}$ of the clumps tend to vary proportionately with the global dust corrected SFR $\text{SFR}_{\text{FUV}}^{\text{corr}}$ (Table 2) of the corresponding objects rather than the local mean dust corrected SFR of the clumps (Table 3). We have spatially constrained the extent of star-forming regions in these galaxies, which is evident from the variation of clump SFR ($M_{\odot} \text{yr}^{-1}$) with radius r_{d} (kpc) in Fig. 3 (Last row). NGC 1961 shows a maximum extent of star formation up to ~ 50 kpc with only a few structures after ≥ 30 kpc, and on the other extent, NGC 1030 shows very few structures extending only up to ~ 12 kpc. The peaks of the clump SFR variation can be seen from the figure denoting spikes in the number of clumps in the spirals arms of the galaxies, which is more evident for objects like NGC 1961 and NGC 266 due to their face-on view.

It can be seen that the young star-forming clumps in these massive galaxies that are spatially resolved through UVIT FUV images show

a local star formation rate density $\Sigma_{\text{SFR}}^{\text{FUV}}$ varying over an order or 10, ranging from approximately $10^{-2} - 10^{-1} M_{\odot} \text{yr}^{-1} \text{kpc}^{-2}$ (Table 2, Fig. 3) even though their global star formation rate density considering the corrected FUV star formation within aperture mentioned in Table 2 varies in the range $\sim 10^{-3.7} - 10^{-2.7} M_{\odot} \text{yr}^{-1} \text{kpc}^{-2}$ signify the fact that the star formation in these massive spirals are highly localised with young star formation going on only locally throughout the galaxy similar to the giant SB0/a Low Surface Brightness (LSB) galaxy Malin1 (Saha et al. 2021). This can further be investigated in detail with sensitive $H\alpha$ observations of these objects.

4.3 Stellar and Interstellar components

The less dust-affected near-infrared K-band luminosity can be taken as a proxy for the stellar mass of galaxies. Estimating the mass-to-light ratio Y_{K}^{\star} of the objects using Bell et al. (2003) based on their color (B-V) (we use u-g in the absence of B-V for NGC 1030 and NGC 5635), the galaxies are found to be extremely massive with stellar masses of the order of a few $\times 10^{11} M_{\odot}$. The masses M_{K} and the corresponding K-band mass-to-light ratios Y_{K}^{\star} (each < 1) are shown in Table 2. It is also important to note that the K-band stellar masses show approximately the same results as the masses calculated from the spectral energy distribution of the objects (Table 5, Fig. 5).

The interstellar medium (ISM) of a galaxy consists of atomic HI, molecular H_2 gas components, and dust. Hydrogen gas components in the ISM can be thought to be enveloping the young star-forming regions, with ionised hydrogen gas existing in the inner region surrounding the star-forming cloud and the atomic and molecular hydrogen gas occupying the middle and outer regions, respectively. To calculate the atomic HI gas mass, we consider the HI integrated line flux from the 21 cm line profile (Tift & Cocke 1988; Springob et al. 2005; Haynes et al. 2011) of the objects. The atomic gas mass M_{HI} can be calculated using the following relation,

$$M_{\text{HI}} = 2.356 \times 10^5 \times D^2 \times (1+z)^{-2} \times \int S_{\nu} d\nu \quad (5)$$

Here, D is the distance to the object in Mpc, z is the redshift, and $\int S_{\nu} d\nu$ is the integrated line flux in Jy km s^{-1} . The galaxy HI gas masses are found to be $\approx 10^{10} M_{\odot}$ for our objects. The HI gas mass is tabulated in Table 2.

Now, to estimate the molecular gas content of our objects, we use the morphology-dependent relation between the molecular and atomic gas mass ($M_{\text{H}_2}/M_{\text{HI}}$) provided by Young & Knezek (1989). Depending on the morphological classifications of the objects as Sa to Sc types (Makarov et al. 2014) we estimate the molecular gas mass to be around $\sim 10^{10} M_{\odot}$ (Table 2) for the objects. Note that, here we have assumed that the molecular gas content of an intermediate bar type (SABb) spiral and a barred Sab spiral does not differentiate much from a non-barred Sab spiral to calculate the molecular gas content for the object NGC 1961 and NGC 266. The total gas mass of the objects is then calculated as $M_{\text{gas}} = 1.38 \times (M_{\text{HI}} + M_{\text{H}_2})$.

The dust mass for the objects is calculated from the spectral energy distribution (Fig. 5) using the model provided by Draine et al. (2014). The estimated mass M_{dust} for the objects fall between $\approx 10^{7-8} M_{\odot}$ (Table 5). The total baryonic mass ($M_{\text{baryon}} = M_{\star} + M_{\text{gas}} + M_{\text{dust}}$) of the objects and their baryonic fraction $f_{\text{b},r200}$ upto the virial radius are mentioned in Table 5 (Lower panel). It can be seen that the baryon fraction of these objects up to the virial radius varies from $\sim 0.014 - 0.055$ indicating $\sim 67 - 92$ per cent fewer baryons ('missing baryons') than expected (see Table 5 for $M_{\text{expected}} \sim 10^{12} M_{\odot}$) according to the cosmic baryon fraction of 0.167. The most significant explanation of

these ‘missing baryons’ has been answered by the X-ray detection of hot gas around these massive galaxies that contribute significantly to the total baryonic mass. Now, if we consider the isothermal (constant temperature) profile of the halo gas, then the virial temperature T_{vir} of the halo gas as a function of the flat circular rotation velocity v_c can be expressed as,

$$T_{\text{vir}} = 35.9 \times \left(\frac{v_c}{\text{km s}^{-1}} \right)^2 \text{ K} \quad (6)$$

Using the circular velocities mentioned in Table 2, we estimate the halo gas temperatures to be of the order of a *few* $\times 10^6 \text{K}$ translating to $0.3 - 0.5 \text{keV}$ (Table 2) for our objects.

According to Kelly et al. (2021), the hot gas ($> 5 \times 10^5 \text{K}$) starts to dominate the total baryon fraction of a galaxy for virial mass beyond $10^{12} M_{\odot}$, who investigated the X-ray gas surrounding galaxies with halo mass in the range $10^{11} - 10^{14} M_{\odot}$ in the cosmological EAGLE simulations. If we consider the virial mass of our objects ($\sim 10^{13} M_{\odot}$), then the ratio of the hot gas to stellar mass component becomes ~ 5 at red-shift $z = 0$ (see Figure 1; Kelly et al. 2021), which gives us hot gas mass around $\sim 10^{12} M_{\odot}$ for the stellar mass of our objects (Table 5) solving the ‘missing baryon’ problem keeping in mind uncertainties in individual parameters. But this vast amount of hot gas has not been seen in massive spirals due to the low density of the hot gas limiting X-ray observations to $\sim 1/5$ th of the virial radius (Mirakhor et al. 2021). In our sample of massive spirals, out of the five objects, two have reported detections of hot ($\sim 10^6 \text{K}$) X-ray halos extending much beyond their optical radius and/or the stellar disc. Bogdán et al. (2013a) detected hot gas emission up to $\sim 60 \text{kpc}$ for NGC 1961 based on XMM-Newton X-ray observations with the hot halo gas mass of $\sim (1.2 \pm 0.2) \times 10^{10} M_{\odot}$ and in Bogdán et al. (2013b) they report hot gas emission upto $\sim 70 \text{kpc}$ containing a mass of $\sim (9.1 \pm 0.9) \times 10^9 M_{\odot}$ using ROSAT and Chandra X-ray observations of NGC 266. These detections give us a hot halo gas mass of 2 orders of magnitude less than what is expected ($\sim 10^{12} M_{\odot}$). The high temperature ($\gtrsim 10^6 \text{K}$) (Table 2) and the low-density halo gas significantly affect the star formation in the host galaxy by not being able to settle down in the galactic disc at temperature $< 10^2 \text{K}$ necessary for forming molecular clouds capable of forming stars.

4.4 Black hole and its effect on star formation

The massive galaxies are often hosts to supermassive black holes at their centres (Magorrian et al. 1998; Gebhardt et al. 2000). It is extremely difficult to constrain the black hole masses of galaxies observationally. So, in order to estimate the black hole mass of the target objects, we use the tight correlation between the mass of the black hole M_{bh} and the central velocity dispersion σ of the spirals (Gültekin et al. 2009). The relation is shown below,

$$\log\left(\frac{M_{\text{bh}}}{M_{\odot}}\right) = (8.12 \pm 0.08) + (4.24 \pm 0.41) \log\left(\frac{\sigma}{200 \text{km s}^{-1}}\right) \quad (7)$$

The central velocity dispersion σ of the objects is mentioned in Table 2. In case the information about the central velocity dispersion is not available for the objects, such as the case for NGC 1030 and NGC 5635, we estimate the black hole mass M_{bh} from the relation provided by Reines & Volonteri (2015) correlating the black hole mass with the stellar mass (see Table 5 for stellar mass). From these relations, we show that the black hole mass of our objects is in the range of a *few* $\times 10^{7-8} M_{\odot}$ and is tabulated in Table 2.

The star formation in massive galaxies ($\geq 10^{11} M_{\odot}$) is still and primarily an unexplored phenomenon; galaxies of such types can be

broadly classified into two groups where a group of galaxies showing extremely quenched SFRs and the other group showing a moderate star formation (Fig. 6, Left panel) for a similar mass range. The massive galaxies are supposed to have acquired much of their stellar mass content before normal main-sequence spirals, which are still actively forming stars, which also determined their growth of central black hole at a faster rate, which is evident from the study carried out by Reines & Volonteri (2015) on a sample of 341 galaxies including galaxies hosting active galactic nuclei (AGN) and inferred that, the growth of black hole mass is accompanied by the growth of stellar mass of the host galaxy, i.e. $M_{\star} \propto M_{\text{bh}}$. As we have discussed in Section 4.1 that, depending on our assumed models, these massive galaxies have experienced their peak in the star-forming activity approximately in the period of red-shift $z \sim 2.4 - 6.5$ (Table 5), reaching up to the ‘cosmic high noon’ at $z \sim 1 - 3$, which overlaps with the ‘quasar epoch’ around red-shift $z \sim 2$. This suggests the coexistence of the era of intense star formation with the ‘quasar epoch’ in the universe (Shaver et al. 1999). However, from the star formation history of our objects, it is evident that there existed a period of rapid star formation assisted by the black holes’ growth as well as rapid stellar mass growth in the pre-quasar era leading up to the ‘quasar epoch’ (Alexander et al. 2005). It indicates the possibility that the rise of star formation in these galaxies and the steep growth of the central black hole mass stops at around the peak of the star formation history of the galaxies, as by then, the black hole must have experienced a growth upto $\sim 10^7 - 10^8 M_{\odot}$ to be able to regulate star formation of the host galaxies efficiently.

Now, we discuss the possible growth scenario of the central black holes in these massive galaxies in their early period of evolution. If the black hole mass at time t is $M_{\text{bh}}(t)$, then the dimensionless Eddington luminosity ratio $\lambda (= L/L_{\text{Edd}})$ can be defined as (Shapiro 2005; Hopkins et al. 2006),

$$\lambda = \frac{\epsilon_r t_{\text{sal}}}{t(1 - \epsilon_r)} \log_e \frac{M_{\text{bh}}(t)}{M_{\text{bh}}(0)} \quad (8)$$

Here, $M_{\text{bh}}(0)$ is the initial black hole mass at time $t = 0$, $\epsilon_r = 0.06 - 0.42$, for spin $0 - 1$ respectively, denotes how efficiently can the accreted mass be converted into radiative energy, $t_{\text{sal}} = 0.45 \text{Gyr}$, the Salpeter timescale. For a scenario of the rapid growth of stellar mass (hence high SFR) and M_{bh} , we expect the radiative efficiency ϵ_r to be smaller as higher ϵ_r will lead to lower growth rate for the black hole mass following above equation, $dM_{\text{bh}}/dt \propto (1/\epsilon_r - 1)$. In our calculations we consider, $\epsilon_r \sim 0.1$ and $M_{\text{bh}}(0)$ to be $10^2 M_{\odot}$, a Population-III seed black hole. If we consider the central black holes of our spirals to have grown up to $\sim 10^8 M_{\odot}$ around the peak of their consequent star formations, then we estimate the ratio λ to be in the range $\sim 0.25 - 0.86$ for $\tau_{\text{main}} \sim 2.8 - 0.8 \text{Gyr}$ (Table 5), i.e. with $\lambda \sim (1/\tau_{\text{main}})$ the accretion approaches the near-Eddington limit ($\lambda \sim 1$) for galaxies experiencing star forming peak sooner ($< 10^9 \text{yr}$) after the ‘Big Bang’. So, It can be seen that the black hole growth and the star formation in a galaxy are closely related to each other, and our results follow the findings of Martín-Navarro et al. (2018), who suggest that the black hole growth in the early universe is proportional to the gas cooling rate and hence the star-forming activity and galaxies hosting more massive black holes experience the suppression of star formation earlier than the others in their later period of evolution. However, from the SED fitting of these objects, we find almost no activity of the active galactic nuclei of these objects in the present time, which is also evident from the AGN class of the objects as mentioned in Table 2. As we do not see any large-scale radio jets from the centre of these objects, we infer that these AGNs

are presently in radio-quiet mode, with possibly weak and small-scale outflows, with no significant effect on the star formation in the galactic disc.

4.5 Star forming efficiency

How efficiently the hot halo baryonic mass is converted into the stellar mass of a galaxy can be characterised by star formation efficiency. The star formation efficiency SFE of a galaxy is defined as the following (Posti et al. 2019),

$$f_{\star} = \frac{M_{\star}}{f_b M_{\text{halo}}} \quad (9)$$

Here, M_{\star} and M_{halo} are the stellar and halo mass of a galaxy, whereas f_b is the cosmic baryon fraction taken as 0.167 in our calculations (Komatsu et al. 2011). To calculate SFE, we use the stellar masses from the best-fit SEDs of the objects (Table 5), and the halo masses of our objects are estimated using the following relations,

$$M_{\text{halo}} = \frac{4}{3} \pi r_{\text{vir}}^3 \Delta_c \rho_c; \text{ where, } r_{\text{vir}} = \frac{GM_{\text{halo}}}{v_{\text{rot}}^2} \ \& \ \rho_c = \frac{3H^2(z)}{8\pi G} \quad (10)$$

Here, we assume that the density of the halo is $\Delta_c \rho_c$ with $\Delta_c \sim 200$ and ρ_c as the critical density of the universe. Under the assumption of flat circular rotational velocity v_{rot} up to the virial radius r_{vir} , the halo mass can be written as, $M_{\text{halo}} = \frac{v_{\text{rot}}^3}{10GH(z)}$; G = Gravitational constant and $H(z)$ = Hubble parameter. Expressing the redshift dependent Hubble parameter as, $H(z) = H_0[\Omega_M(1+z)^3 + \Omega_{\text{vac}}]^{1/2}$, the halo masses are estimated as $few \times 10^{13} M_{\odot}$ (see Section 1 for H_0 , Ω_M and Ω_{vac}). The estimated halo masses and SFEs are shown in Table 2 and Table 5, respectively. The star-forming efficiency of our sample of the massive spirals is shown in (Fig. 6, right panel) along with other massive spirals like UGC 12591 (Ray et al. 2022) and J2345-0449 (Bagchi et al. 2014; Nesvadba et al. 2021). We also show the SPARC (Spitzer Photometry and Accurate Rotation Curves) sample of disc galaxies from Lelli et al. (2016) having stellar mass in the range of $\sim 10^7$ to $> 10^{11} M_{\odot}$ in the graph. The star formation efficiency of the galaxies is supposed to peak around the stellar mass of $M_{\star} \sim 10^{10.2-10.3} M_{\odot}$ with $f_{\star} \sim 20$ per cent (Moster et al. 2013). This means that massive galaxies in their evolution towards the stellar mass of $\sim 10^{11} M_{\odot}$ can only experience a maximum ~ 20 per cent SFE with most of their baryons not converted into stars. However, the massive spirals from Lelli et al. (2016); Ogle et al. (2019b), as shown in the graph, depict a contradictory trend at the high mass end where the SFE increases with increasing stellar mass upto $> 10^{11} M_{\odot}$ and corresponding f_{\star} reaching $\approx 0.3-1$ indicating the conversions of the most (30–100 per cent) of their baryons into stars. In contrast to this, an extremely massive, quenched and isolated spiral like UGC 12591 shows an SFE of $\sim 3-5$ per cent and falls in the place expected from Moster et al. (2013) model for red-shift $z \sim 0$. Our sample set of massive spirals with even greater stellar masses than the other samples mentioned before shows a star-forming efficiency of $\sim 7-30$ per cent with NGC 4501 and NGC 5635 having the highest and the lowest f_{\star} respectively (Table 5) indicating a moderate to low ongoing ($z \sim 0$) conversions of baryons into stars. As we have discussed before in Section 4.1, our objects fall in the ‘Green Valley’ region considering some signatures of recent star formation as evident from Fig. 6 (left panel) arguably induced by interactions. However, they fall below the star formation efficiency line for $f_{\star} = 1$, the line showing all baryons have been converted into stars. Moreover, they have higher SFEs than expected from the stellar-to-halo mass relation

provided by Moster et al. (2013) by abundance matching model (Fig. 6, right panel). This indicates the possibility that the stellar masses of these objects may have grown recently due to turbulence-induced star formation in the disc and possible gas inflow to some extent; however, large-scale baryon cooling and/or halo gas ($\sim 10^6 K$) condensation in the galactic disc is not very predominant provided their baryon fractions $f_{b,r200}$ (Table. 5) are much less than the cosmic baryon fraction.

5 CONCLUSIONS

In this paper, we study the aspects related to star formation in massive spirals ($> L_{\star}$) with a focus on five late-type galaxies NGC 1030, NGC 1961, NGC 4501, NGC 5635 and NGC 266 observed in UltraViolet Imaging Telescope onboard ASTROSAT. In addition to analysing the UVIT data, we used the archival data of GALEX, SDSS, PanSTARRS, DECaLS, 2MASS, WISE and IRAS in our analysis. The significant results of our analysis are listed below:

(i) The late-type spiral galaxies show a mix of moderate to nearly quenched young (~ 100 Myr) FUV star formation. Taking dust correction into account NGC 1961 show the highest star formation of $\text{SFR}_{\text{FUV}}^{\text{corr}} = 13.66 \pm 2.04$ followed by NGC 4501 with $\text{SFR}_{\text{FUV}}^{\text{corr}} = 13.51 \pm 2.24 M_{\odot} \text{yr}^{-1}$ and the other three galaxies NGC 1030, NGC 5635 and NGC 266 show $\text{SFR}_{\text{FUV}}^{\text{corr}} = 5.15 \pm 0.87, 1.43 \pm 0.13$ and $2.54 \pm 0.25 M_{\odot} \text{yr}^{-1}$ respectively.

(ii) We identify the young star-forming regions in the galaxies within a defined aperture, considering them to be hierarchical in nature and segregating them into clumps. We find that the star formation in these galaxies is highly localised with star formation rate density $\Sigma_{\text{SFR}}^{\text{FUV}}$ in the range of $\sim 10^{-2} - 10^{-1} M_{\odot} \text{yr}^{-1} \text{kpc}^{-2}$ as opposed to a global star formation rate density of $\sim 10^{-3.7} - 10^{-2.7} M_{\odot} \text{yr}^{-1} \text{kpc}^{-2}$.

(iii) From the FUV-FIR multi-wavelength SED fitting of each of the galaxies, we find the stellar mass M_{\star} of the objects to be of the order of a $few \times 10^{11} M_{\odot}$ with instantaneous star formation falling in the ‘green valley’ region with $10^{-11.5} < \text{sSFR} (M_{\odot} \text{yr}^{-1}) < 10^{-10.5}$ and with SFR_{inst} in the range $\sim 1.7 - 12.0 M_{\odot} \text{yr}^{-1}$. We find no significant AGN contributions affecting the star formation of these objects in the present era. However, all our objects show a varying degree of asymmetry/interactions, which most probably explains the recent star formation activity in these objects.

(iv) Based on a delayed star formation history model, the peak of the star formation history of the objects is found to be in the range $\sim 0.8 - 2.8$ Gyr after the ‘Big Bang’ expanding throughout pre-cosmic ‘high noon’ and pre-quasar era ($1 < z < 3$). The galaxies that had experienced peaks sooner after the ‘Big Bang’ show relatively low star formation at low redshift ($z \sim 0$) than the others. For example, NGC 1030 and NGC 5635 experienced their peak ~ 0.843 Gyr after the ‘Big Bang’ have low instantaneous star formation rates of 1.66 ± 0.08 and $1.29 \pm 0.06 M_{\odot} \text{yr}^{-1}$, whereas, NGC 1961 shows a relatively higher instantaneous star formation of $12.04 \pm 2.48 M_{\odot} \text{yr}^{-1}$ having experienced the peak ~ 2.75 Gyr after the ‘Big Bang’.

(v) We show that the objects had gained much of their stellar mass ($> 10^{11} M_{\odot}$) very rapidly in the early period of their evolution, acquiring almost $\sim 31 - 42$ per cent of the present-day stellar mass in a period of $\sim (1/16) - (1/5)^{\text{th}}$ of the age of the Universe. We

argue that the early period of growth of the central black holes in these objects occurred rapidly with star formation and stellar mass growth in these objects. We show that the black holes must have accreted at near Eddington limit for objects that had their peak in the star formation at around $\lesssim 10^9$ yrs after the ‘Big Bang’ to be able to grow up to $10^8 M_\odot$ and affect star formation activity of the host.

(vi) We find that these spirals have baryonic mass (a *few* $\times 10^{11} M_\odot$) of $\sim 67 - 92$ per cent less than what is expected (a *few* $\times 10^{12} M_\odot$) from the cosmic baryon fraction of 0.167. X-ray hot halo mass detected in two objects, NGC 1961 and NGC 266, tries to compensate for the ‘missing baryons’; however, they still are far less than what is expected. These objects have star-forming efficiency, the baryon-to-star conversion efficiency in the range $\sim 7 - 31$ per cent with halo mass of $> 10^{13} M_\odot$ and hot halo gas temperature of $\sim 10^6$ K. With baryon fraction f_b , r_{200} far less than 0.167, we conclude that there is no large scale baryon cooling happening in these extremely massive objects.

ACKNOWLEDGEMENTS

The authors are grateful to the anonymous referee for the encouraging and constructive comments on the manuscript, which greatly helped us in improving its quality. This publication uses the data from the UVIT, which is part of the ASTROSAT mission of the ISRO, archived at the Indian Space Science Data Centre (ISSDC). We thank Dr. Kanak Saha for his help during the observation proposal writing of target galaxies to the ASTROSAT. SR gratefully acknowledges the support from the Department of Physics and Electronics, CHRIST (Deemed to be University), Bangalore and funding by the Indian Space Research Organisation (ISRO) under ‘AstroSat Data Utilization’ project. SD acknowledges support from the Indian Space Research Organisation (ISRO) funding under project PAO/REF/CP167. JB acknowledges the support from the Department of Physics and Electronics, CHRIST (Deemed to be University), Bangalore. MBP gratefully acknowledges the support from the following funding schemes: The Science and Engineering Research Board (SERB), New Delhi, under the SERB ‘SERB’ Research Scientists Scheme Scheme and Indian Space Research Organisation (ISRO) under the ‘AstroSat Data Utilization’ project. MBP also acknowledges the support from IUCAA Associateship programme. We acknowledge the usage of the HyperLeda database (<http://leda.univ-lyon1.fr>). This research has made use of NASA’s Astrophysics Data System and of the NASA/IPAC Extragalactic Database (NED), which is operated by the Jet Propulsion Laboratory, California Institute of Technology, under contract with the National Aeronautics and Space Administration. This research has made use of the VizieR catalogue access tool, CDS, Strasbourg, France (DOI : 10.26093/cds/vizie). The original description of the VizieR service was published in 2000, *A&AS* 143, 23

DATA AVAILABILITY

The UVIT data used in this work is publicly available at https://webapps.issdc.gov.in/astro_archive/archive/Home.jsp. The other archival data used are available in the following links: GALEX: <https://mast.stsci.edu/portal/Mashup/Clients/Mast/Portal.html>, SDSS: <https://dr12.sdss.org/mosaics>, Pan-STARRS:

<https://outerspace.stsci.edu/display/PANSTARRS/>, DECaLS: <https://www.legacysurvey.org/>, 2MASS, WISE and IRAS: <https://irsa.ipac.caltech.edu/frontpage/>. The softwares used for data analysis are available at, CCD-LAB: <https://github.com/user29A/CCDLAB>, ASTRODENDRO: <https://dendrograms.readthedocs.io/en/stable/>, <https://github.com/dendrograms/astrodendro>, CIGALE: <https://cigale.lam.fr/>, <https://gitlab.lam.fr/cigale/cigale/>.

REFERENCES

- Alexander D. M., Hickox R. C., 2012, *New Astron. Rev.*, **56**, 93
 Alexander D. M., Smail I., Bauer F. E., Chapman S. C., Blain A. W., Brandt W. N., Ivison R. J., 2005, *Nature*, **434**, 738
 Bagchi J., et al., 2014, *ApJ*, **788**, 174
 Behroozi P. S., Conroy C., Wechsler R. H., 2010, *ApJ*, **717**, 379
 Behroozi P., Wechsler R. H., Hearin A. P., Conroy C., 2019, *MNRAS*, **488**, 3143
 Bell E. F., McIntosh D. H., Katz N., Weinberg M. D., 2003, *ApJS*, **149**, 289
 Benson A. J., 2010, *Phys. Rep.*, **495**, 33
 Bertin E., 2010, SWarp: Resampling and Co-adding FITS Images Together, Astrophysics Source Code Library, record ascl:1010.068 (ascl:1010.068)
 Bertin E., Arnouts S., 1996, *A&AS*, **117**, 393
 Bertin E., Mellier Y., Radovich M., Missonnier G., Didelon P., Morin B., 2002, in Bohlender D. A., Durand D., Handley T. H., eds, *Astronomical Society of the Pacific Conference Series Vol. 281, Astronomical Data Analysis Software and Systems XI*. p. 228
 Birnboim Y., Dekel A., 2003, *MNRAS*, **345**, 349
 Bogdán Á., et al., 2013a, *ApJ*, **772**, 97
 Bogdán Á., Forman W. R., Kraft R. P., Jones C., 2013b, *ApJ*, **772**, 98
 Boquien M., Burgarella D., Roehlly Y., Buat V., Ciesla L., Corre D., Inoue A. K., Salas H., 2019, *A&A*, **622**, A103
 Bournaud F., 2011, in Charbonnel C., Montmerle T., eds, *EAS Publications Series Vol. 51, EAS Publications Series*. pp 107–131 ([arXiv:1106.1793](https://arxiv.org/abs/1106.1793)), doi:10.1051/eas/1151008
 Bower R. G., Benson A. J., Malbon R., Helly J. C., Frenk C. S., Baugh C. M., Cole S., Lacey C. G., 2006, *MNRAS*, **370**, 645
 Brinchmann J., Charlot S., White S. D. M., Tremonti C., Kauffmann G., Heckman T., Brinkmann J., 2004, *MNRAS*, **351**, 1151
 Brodie J. P., Strader J., 2006, *ARA&A*, **44**, 193
 Bruzual G., Charlot S., 2003, *MNRAS*, **344**, 1000
 Calzetti D., Armus L., Bohlin R. C., Kinney A. L., Koornneef J., Storchi-Bergmann T., 2000, *ApJ*, **533**, 682
 Cardelli J. A., Clayton G. C., Mathis J. S., 1989, *ApJ*, **345**, 245
 Cheng C., et al., 2023, *ApJ*, **942**, L19
 Cicone C., et al., 2014, *A&A*, **562**, A21
 Cole S., Lacey C. G., Baugh C. M., Frenk C. S., 2000, *MNRAS*, **319**, 168
 Corradi R. L. M., Capaccioli M., 1991, *A&AS*, **90**, 121
 Croton D. J., et al., 2006, *MNRAS*, **365**, 11
 Dai X., Anderson M. E., Bregman J. N., Miller J. M., 2012, *ApJ*, **755**, 107
 Dekel A., Sari R., Ceverino D., 2009, *ApJ*, **703**, 785
 Dhiwar S., Saha K., Dekel A., Paswan A., Pandey D., Cortesi A., Pandge M., 2023, *MNRAS*, **518**, 4943
 Draine B. T., et al., 2014, *ApJ*, **780**, 172
 Elbaz D., et al., 2007, *A&A*, **468**, 33
 Feldmann R., Mayer L., 2015, *MNRAS*, **446**, 1939
 Förster Schreiber N. M., et al., 2014, *ApJ*, **787**, 38
 Fritz J., Franceschini A., Hatziminaoglou E., 2006, *MNRAS*, **366**, 767
 Fukugita M., Peebles P. J. E., 2006, *ApJ*, **639**, 590
 Garrido O., Marcellin M., Amram P., Balkowski C., Gach J. L., Boulesteix J., 2005, *MNRAS*, **362**, 127
 Gebhardt K., et al., 2000, *ApJ*, **539**, L13
 Gil de Paz A., et al., 2007, *ApJS*, **173**, 185
 Gott J. R. I., 1977, *ARA&A*, **15**, 235
 Gottesman S. T., Hunter J. H. J., Shostak G. S., 1983, *MNRAS*, **202**, 21P

- Gültekin K., et al., 2009, *ApJ*, **698**, 198
- Haynes M. P., et al., 2011, *AJ*, **142**, 170
- Helou G., Khan I. R., Malek L., Boehmer L., 1988, *ApJS*, **68**, 151
- Hibbard J. E., van Gorkom J. H., Rupen M. P., Schiminovich D., 2001, in Hibbard J. E., Rupen M., van Gorkom J. H., eds, *Astronomical Society of the Pacific Conference Series Vol. 240, Gas and Galaxy Evolution*. p. 657 ([arXiv:astro-ph/0110667](https://arxiv.org/abs/astro-ph/0110667)), doi:10.48550/arXiv.astro-ph/0110667
- Hoopes C. G., et al., 2007, *ApJS*, **173**, 441
- Hopkins P. F., Narayan R., Hernquist L., 2006, *The Astrophysical Journal*, **643**, 641
- Huang J. S., et al., 2023, [arXiv e-prints](https://arxiv.org/abs/2304.01378), p. [arXiv:2304.01378](https://arxiv.org/abs/2304.01378)
- Inoue A. K., 2011, *MNRAS*, **415**, 2920
- Joye W. A., Mandel E., 2003, in Payne H. E., Jedrzejewski R. I., Hook R. N., eds, *Astronomical Society of the Pacific Conference Series Vol. 295, Astronomical Data Analysis Software and Systems XII*. p. 489
- Kalinova V., Colombo D., Sánchez S. F., Kodaira K., García-Benito R., González Delgado R., Rosolowsky E., Lacerda E. A. D., 2021, *A&A*, **648**, A64
- Kaviraj S., et al., 2007, *ApJS*, **173**, 619
- Kelly A. J., Jenkins A., Frenk C. S., 2021, *MNRAS*, **502**, 2934
- Kenicutt Robert C. J., 1998, *ARA&A*, **36**, 189
- Kenicutt R. C., Evans N. J., 2012, *ARA&A*, **50**, 531
- Komatsu E., et al., 2011, *ApJS*, **192**, 18
- Labbe I., et al., 2022, [arXiv e-prints](https://arxiv.org/abs/2207.12446), p. [arXiv:2207.12446](https://arxiv.org/abs/2207.12446)
- Lackner C. N., Cen R., Ostriker J. P., Joung M. R., 2012, *MNRAS*, **425**, 641
- Lelli F., McGaugh S. S., Schombert J. M., 2016, *AJ*, **152**, 157
- Lütticke R., Pohlen M., Dettmar R. J., 2004, *A&A*, **417**, 527
- Madau P., Dickinson M., 2014, *ARA&A*, **52**, 415
- Magorrian J., et al., 1998, *AJ*, **115**, 2285
- Makarov D., Prugniel P., Terekhova N., Courtois H., Vauglin I., 2014, *A&A*, **570**, A13
- Man A., Belli S., 2018, *Nature Astronomy*, **2**, 695
- Martín-Navarro I., Brodie J. P., Romanowsky A. J., Ruiz-Lara T., van de Ven G., 2018, *Nature*, **553**, 307
- Mathis J. S., Rumpf W., Nordsieck K. H., 1977, *ApJ*, **217**, 425
- McGaugh S. S., 2005, *ApJ*, **632**, 859
- Mirakhor M. S., et al., 2021, *MNRAS*, **500**, 2503
- Moster B. P., Naab T., White S. D. M., 2013, *MNRAS*, **428**, 3121
- Naab T., Ostriker J. P., 2017, *ARA&A*, **55**, 59
- Nesvadba N. P. H., et al., 2021, *A&A*, **654**, A8
- Ogle P. M., Lanz L., Appleton P. N., Helou G., Mazzarella J., 2019a, *The Astrophysical Journal Supplement Series*, **243**, 14
- Ogle P. M., Jarrett T., Lanz L., Cluver M., Alatalo K., Appleton P. N., Mazzarella J. M., 2019b, *ApJ*, **884**, L11
- Oser L., Ostriker J. P., Naab T., Johansson P. H., Burkert A., 2010, *ApJ*, **725**, 2312
- Park M., et al., 2023, *ApJ*, **953**, 119
- Pearson W. J., et al., 2019, *A&A*, **631**, A51
- Posti L., Fraternali F., Marasco A., 2019, *A&A*, **626**, A56
- Postma J. E., Leahy D., 2017, *PASP*, **129**, 115002
- Ray S., Bagchi J., Dhiwar S., Pandge M. B., Mirakhor M., Walker S. A., Mukherjee D., 2022, *MNRAS*, **517**, 99
- Rees M. J., Ostriker J. P., 1977, *MNRAS*, **179**, 541
- Reines A. E., Volonteri M., 2015, *ApJ*, **813**, 82
- Renzini A., Peng Y.-j., 2015, *ApJ*, **801**, L29
- Robertson B. E., 2022, *ARA&A*, **60**, 121
- Robitaille T., Rice T., Beaumont C., Ginsburg A., MacDonald B., Rosolowsky E., 2019, *astrodendro: Astronomical data dendrogram creator*, *Astrophysics Source Code Library*, record ascl:1907.016 (ascl:1907.016)
- Rodríguez-Gomez V., et al., 2016, *MNRAS*, **458**, 2371
- Rubin V. C., Ford W. K. J., Roberts M. S., 1979, *ApJ*, **230**, 35
- Saglia R. P., Sancisi R., 1988, *A&A*, **203**, 28
- Saha K., Dhiwar S., Barway S., Narayan C., Tandon S., 2021, *Journal of Astrophysics and Astronomy*, **42**, 59
- Salim S., et al., 2016, *ApJS*, **227**, 2
- Salpeter E. E., 1955, *ApJ*, **121**, 161
- Schlafly E. F., Finkbeiner D. P., 2011, *ApJ*, **737**, 103
- Schultz G. V., Wiemer W., 1975, *A&A*, **43**, 133
- Shapiro S. L., 2005, *The Astrophysical Journal*, **620**, 59
- Shaver P. A., Hook I. M., Jackson C. A., Wall J. V., Kellermann K. I., 1999, in Carilli C. L., Radford S. J. E., Menten K. M., Langston G. I., eds, *Astronomical Society of the Pacific Conference Series Vol. 156, Highly Redshifted Radio Lines*. p. 163 ([arXiv:astro-ph/9801211](https://arxiv.org/abs/astro-ph/9801211)), doi:10.48550/arXiv.astro-ph/9801211
- Shostak G. S., Hummel E., Shaver P. A., van der Hulst J. M., van der Kruit P. C., 1982, *A&A*, **115**, 293
- Somerville R. S., Davé R., 2015, *ARA&A*, **53**, 51
- Sommer-Larsen J., 2006, *ApJ*, **644**, L1
- Springob C. M., Haynes M. P., Giovanelli R., Kent B. R., 2005, *ApJS*, **160**, 149
- Tandon S. N., et al., 2017, *AJ*, **154**, 128
- Thomas D., Maraston C., Bender R., Mendes de Oliveira C., 2005, *ApJ*, **621**, 673
- Thomas D., Maraston C., Schawinski K., Sarzi M., Silk J., 2010, *MNRAS*, **404**, 1775
- Tift W. G., Cocke W. J., 1988, *ApJS*, **67**, 1
- Tody D., 1986, in Crawford D. L., ed., *Society of Photo-Optical Instrumentation Engineers (SPIE) Conference Series Vol. 627, Instrumentation in astronomy VI*. p. 733, doi:10.1117/12.968154
- Vollmer B., Soida M., Chung A., van Gorkom J. H., Otmianowska-Mazur K., Beck R., Urbanik M., Kenney J. D. P., 2008, *A&A*, **483**, 89
- Wechsler R. H., Tinker J. L., 2018, *ARA&A*, **56**, 435
- White S. D. M., Frenk C. S., 1991, *ApJ*, **379**, 52
- White S. D. M., Rees M. J., 1978, *MNRAS*, **183**, 341
- Xu K., Liu C., Jing Y., Wang Y., Lu S., 2020, *ApJ*, **895**, 100
- Yang G., et al., 2022, *ApJ*, **927**, 192
- Young J. S., Knezek P. M., 1989, *ApJ*, **347**, L55

This paper has been typeset from a $\text{\TeX}/\text{\LaTeX}$ file prepared by the author.